University of Groningen

Master Research Project

Laser Cooling of Barium Monofluoride: Detailed Simulation Studies and Reintroduction of Vibrationally Excited Molecules

Author:
Max Vos

First Supervisor:
Prof. Dr. S. Hoekstra
Second Supervisor:
Dr. S.A. Jones

June, 2024

university of groningen / faculty of science and engineering

Abstract

The cryogenic beam of barium monofluoride molecules in the NL-eEDM experiment is cooled in the transverse direction to increase the statistics of the electron electric dipole moment measurement. First, we simulate laser cooling, using an open-source Python package called PyLCP, to study the effects of detuning, light intensity, and magnetic field on the velocity-force dependence of laser cooling. We find the optimal laser cooling configuration for two velocity regions that are important to the laser cooling experiment. Secondly, we reintroduce molecules that are lost from the main laser cooling transition to vibrationally excited states. The molecules are reintroduced by a laser, with sidebands generated by an electro-optical modulator (EOM). The EOM's modulation depth and driving frequency are optimized so the light beam frequencies overlap with the four hyperfine levels in the first vibrationally excited state.

Contents

1. Context: A tabletop experiment to go beyond the Standard Model

High-precision measurements on properties of Standard Model particles can guide physicists to answer open questions of modern physics. One such question is the apparent matter-antimatter asymmetry in the universe. A contribution to the matter-antimatter asymmetry can be due to violations of the charge-parity conjugation symmetry (CP violation). Many experiments, like the LHCb experiment [19], are currently looking for sources of CP violation. Beyond Standard Model (BSM) theories formulate additions to the Standard Model that include such CP violations.

The NL-eEDM collaboration contributes to the search for CP violations by studying the electron electric dipole moment (eEDM). A non-zero eEDM implies an asymmetric charge distribution around the electron, which is at odds with the time-reversal symmetry (T-violation). In CPT theory, one of the foundations of the Standard Model, T violation is equivalent to CP violation. Recent calculations on the Standard Model say it predicts the electron electric dipole moment to be on the order of $|d_e| \leq O(10^{-35})$ e$\cdot$ cm [9]. This is far beyond the reach of an experimental measurement.

Some BSM theories are based on an eEDM value orders of magnitude higher than the Standard Model prediction. Figure 1.1 provides an overview of the eEDM value predicted by various BSM theories, together with experimentally obtained upper limits of the eEDM. This demonstrates that the eEDM measurements restrict the BSM theories, and can guide towards further development of these theories.

1.1 The NL-eEDM collaboration measuring the eEDM

The NL-eEDM experiment uses the single valence electron of barium monofluoride (BaF) for the precision measurement of the eEDM. The eEDM is determined by looking at the precession frequency of the electron, which presides in a controlled magnetic and electric field called the interaction zone [20]. The BaF molecules produced in a cryogenic buffer-gas source travel at speed through the interaction zone, shown in Figure 1.2.

The advantage of using the valence electron of the BaF molecule over an electron by itself is that the molecule is electrically neutral. A sole electron would be accelerated by the electric field which would complicate the experiment. Furthermore, a diatomic molecule has a molecular enhancement factor: the valence electron experiences an enhanced electric field due to the molecular structure of the diatomic molecule. Due to its quantum properties, BaF is suitable for laser cooling and deceleration by a stark decelerator.

The precision of an eEDM measurement is limited by statistical uncertainty, which is given by [20],

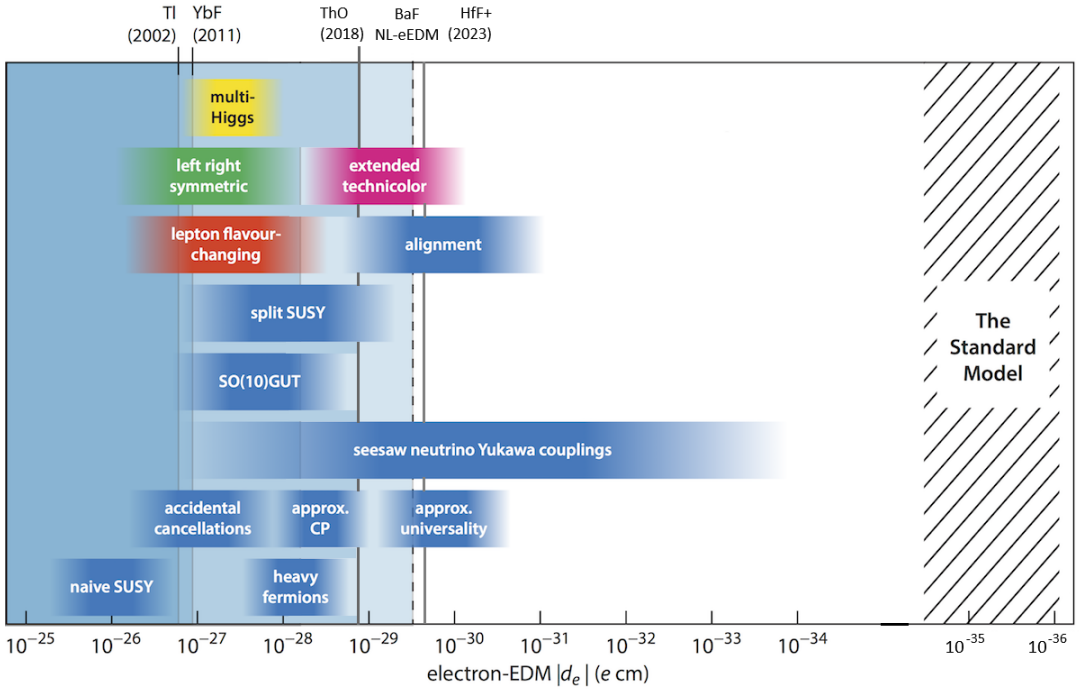

Figure 1.1: The horizontal bars denote the eEDM value as predicted by various beyond Standard Model theories. The vertical lines show the recent experimental results on the upper limit of the eEDM. The dashed vertical line indicates the aim of the NL-eEDM collaboration [8]. (updated)

$$\sigma_d = \frac{\hbar}{E \cdot A \cdot P(E) \cdot \epsilon \cdot T \cdot \sqrt{n}}. \tag{1.1}$$

Here E is the electric field, A is the molecular enhancement factor, $P(E)$ is the molecular polarisation factor, ϵ is the measurement efficiency, T is the interaction time and n is the number of uncorrelated molecules for which the eEDM is measured.

Thus, a method to increase eEDM statistics is to increase T. In other words, the molecules must spend more time interaction zone. This means that the velocity of the molecular beam must be reduced.

1.1.1 Reducing the velocity of the molecular beam

The BaF molecules exit the buffer gas cryogenic source with a longitudinal velocity of $\sim$ 190 m/s and a transverse velocity of $\sim$ 5 m/s. To decrease the longitudinal velocity of the BaF, the NL-eEDM experiment utilizes a Travel-wave Stark decelerator, shown in the purple square in Figure 1.2.

The Traveling-wave Stark decelerator exploits the Stark effect, which is the electric field analog of the Zeeman effect. This means that an electric field causes the energy of a molecule's hyperfine levels to shift up or down. An upward shift induced by the Stark effect is termed "low electric field seeking", which means they prefer to go to lower electric fields. Upon entrance

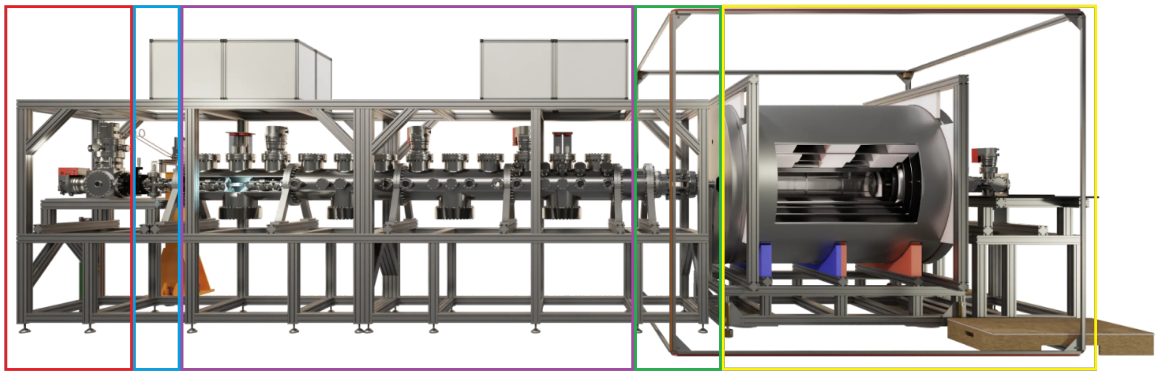

Figure 1.2: An illustration of the proposed setup of the NL-eEDM collaboration. In the red square is the BaF cryogenic buffer gas source. In the blue square is the hexapole electrostatic lens. In the purple square is the traveling wave stark decelerator. In the green square is the laser cooling section. In the yellow square is the interaction zone. Illustration made by A.P. Touwen

into the decelerator, the molecules are captured by a traveling electric potential well. The molecules are attracted to the bottom of the well. It reduces the velocity of the molecule by slowly reducing the velocity of the potential well without losing the molecule [1].

A decrease in molecular longitudinal velocity allows more time for the transverse velocity to move the molecule to the side, out of the transverse acceptance of the experiment. In particular, the molecules must remain within a diameter of 10 mm to enter the interaction zone. It is therefore paramount to decrease the transverse velocity of the molecules. The NL-eEDM experiment achieves this via laser cooling.

1.2 Outline of the thesis

This thesis starts with a theoretical discussion on laser cooling BaF. The energy level structure of BaF is introduced and the subtleties critical to laser cooling are pointed out. Then we discuss all the parameters and design choices of the laser cooling setup that influence the velocities that are laser-cooled.

In the theoretical discussion, we find that one of the subtleties important to laser cooling is the vibrational degree of freedom of BaF. This causes molecules to decay to different energy levels and lose them from the laser cooling transition. In the next chapter, we develop a method to reintroduce these molecules back to the laser cooling transition by an additional laser. An electro-optical modulator adds sidebands to the light field that address the hyperfine levels of the vibrationally excited states.

In the last chapter, we present a study on the Doppler forces using simulations. We define two velocity regions in which we optimize the detuning, light intensity, and magnetic field for maximum cooling. Also, we look at what magnetic field strength and the angle between the magnetic field and light polarization that result in Larmor precession. Then we study an alternative detuning strategy in which only one of the sidebands is detuned. At last, we

reproduce a result from an article by J.A. Devlin and M.R. Tarbutt (2018) [3] to benchmark our simulation technique.

In the appendices, we show some practical additions made to the experiment during this master project.

2. Theoretical framework for laser cooling barium monofluoride

This section provides a theoretical introduction to laser cooling BaF. We show how laser cooling works and introduce the difficulties of laser cooling that lead to the studies shown in Chapter 3 and Chapter 4.

In the first section, the concept of laser cooling is introduced. The velocity regions of Doppler and sub-Doppler forces are discussed. During this discussion, we look at the effect of these forces in a velocity-force curve.

Then follows a discussion of the energy level structure. Laser cooling is a game of clever energy-level transitions. The energy level structure acts as the playing for laser cooling. First, the naming strategy of these energy levels is introduced. The energy level structure of BaF consists of many degrees of freedom, each of which is discussed, and its importance in laser cooling is explained.

Where the energy level structure is the playing field, the laser cooling scheme is the strategy of laser cooling. The laser cooling scheme must be optimized for the velocity range that is cooled. Also, we show methods to maximize the scattering rate. This section is important to understand our work in Chapter 4, where simulations provide insight when designing the laser cooling scheme.

Laser cooling works via the interaction between a light field and a particle, in our case a molecule. In the next section, some phenomena that come with this interaction are introduced.

Finally, the setup of the NL-eEDM laser cooling experiment is introduced.

2.1 Concept of laser cooling

The objective of laser cooling is to reduce the velocity of particles by interaction with a light field. In laser cooling, the force is dependent on the velocity of the particle with respect to the light field. In this section, different forms of laser cooling are introduced and the velocities at which they come into play are specified. Figure 2.1 shows a typical laser cooling velocity-force curve, this figure is explained throughout this section.

2.1.1 Doppler cooling

The simplest form of laser cooling is called Doppler cooling. In Doppler cooling, a particle, initially in a stable ground state, is excited by an interacting photon. A photon interacts if the frequency matches the transition frequency of the two energy levels. The momentum of the photon is thereby absorbed by the particle. After the lifetime of the excited state, it decays to a lower state and emits a photon.

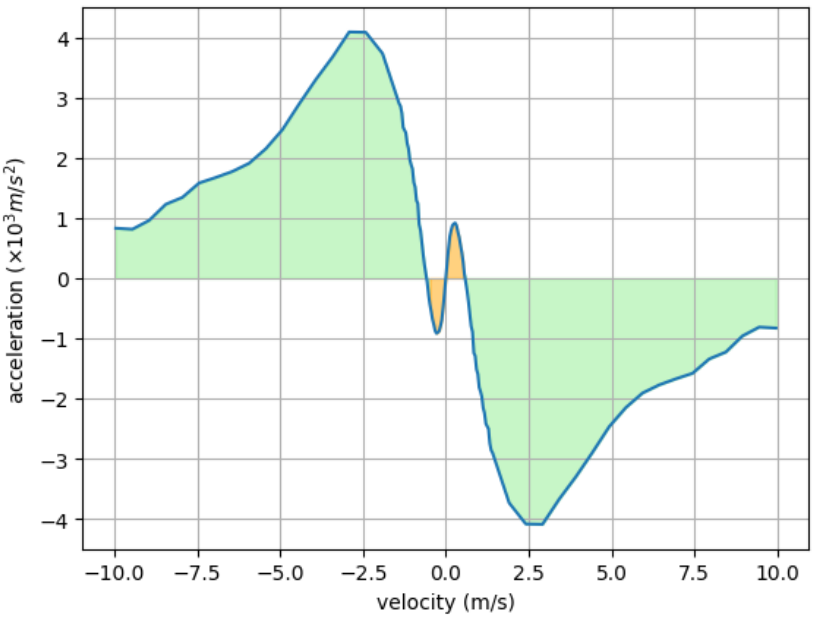

Figure 2.1: An example of a velocity-force curve as a result of laser cooling forces on BaF with a detuning of -1Γ and a light intensity of 5 times the saturation intensity. The light green region indicates the Doppler cooling force and the orange region indicates the sub-Doppler cooling force region. The force is converted to acceleration for intuitive interpretation.

A continuous light field induces this transition many times. The absorbed photon always arrives from the direction of the laser, while the emitted photon has a random direction. After multiple photons, the momentum of the emitted photons cancels out while the absorbed momentum adds up. The laser beam pushes the particles away.

Doppler cooling targets particles that travel towards the laser, this is done by exploiting the Doppler effect. This phenomenon is familiar in the siren of a passing ambulance, and changes the frequency of a light field within the frame of reference of the particle, the degree to which is dependent upon the particle's speed. In Doppler cooling, the light field is slightly detuned from the transition frequency. Particles moving toward the light field see the transition frequency and interact with the light. Other particles do not interact with the light field.

Thus, each time the particle absorbs a photon, its momentum is reduced by that of the photon. In our experiment, the momentum of the single photon reduces the velocity of the particle by about 2.5 mm/s. In total, we desire to reduce the velocity of the particle on the order of 5 m/s. To achieve this, approximately 2000 transitions are needed during the laser cooling section.

Doppler cooling force is shown in the green sections of Figure 2.1. The Doppler cooling force peaks when the velocity of the particle counteracts the detuning of the laser light. In Figure 2.1 where the detuning is -1Γ, a particle with a velocity of 2.3 m/s experiences the light field to be resonant. Therefore the Doppler cooling has its peak around 2.3 m/s. The amount of force around its peak is dependent on the light intensity of the laser. In Figure 2.1, the acceleration is on the order of 3000 m/s^2. If a particle is in this light field for 0.5 ms its transverse velocity

is reduced by 1.5 m/s.

One can see on the left of Figure 2.1, that particles with negative velocity which travel in the same direction as the laser light experience positive acceleration.

Figure 2.1 shows the velocity-force curve for red-detuned light, meaning it is detuned to a frequency below resonant. For blue-detuned light the velocity-force curve of Figure 2.1 would be mirrored in the x-axis. With blue-detuned light, the laser would interact with particles moving away from the laser and increase their velocity.

In Doppler cooling, there is a continuous emission of photons in a random direction. This causes the particle to demonstrate Brownian-like motion, which imposes a lower limit on the temperature that can be reached by Doppler cooling. This is termed the Doppler limit.

2.1.2 Sub-Doppler cooling

Besides Doppler cooling, there exist further complex cooling techniques based on the interaction between light and particles. Generally, these techniques can cool particles to below the Doppler limit, which is why they are called sub-Doppler cooling.

Sub-Doppler forces act in a lower velocity region than Doppler forces. The sub-Doppler forces show up in Figure 2.1 in the orange region.

In section 2.3.2, we see that molecules are cooled by a type-II laser cooling scheme, which means that the ground state has hyperfine levels that are not present in the excited state. Because of this, the sub-Doppler forces act in the opposite direction of Doppler forces, visible in Figure 2.1. As such, Doppler cooling cannot cool particles below the velocity where sub-Doppler forces become dominant, in Figure 2.1 this is at about 0.5 m/s.

The NL-eEDM laser cooling experiment currently does not make use of sub-Doppler forces. This may be a point of interest when we wish to cool to lower velocities.

2.2 Energy levels of a diatomic molecule

Laser cooling is based on transitions between energy levels. In this section, we introduce different categories of energy levels and a naming for them.

The energy levels of a diatomic molecule are categorized by the different degrees of freedom in a diatomic molecule. Firstly, there are the electronic energy levels. Analogous to atoms, these energy levels come from the angular and spin momenta of the nuclei and valence electron of the diatomic molecule. Secondly, there are vibrational energy levels, which come from the vibration of the two atoms with respect to each other. Lastly, there are the rotational energy levels, which come from the rotation of the atoms about each other. These different degrees of freedom each have their importance in laser cooling and have their separate quantum numbers to denote them. The electronic degree of freedom has the largest spacing between energy levels, followed by the vibrational degree of freedom, and then the rotational degree of freedom.

Now, the degrees of freedom are not independent of each other: they are coupled. The coupling

is described by so-called Hund's cases. The naming of each energy level depends slightly on the coupling. For more information on Hund's cases see [1].

In the following sections, each degree of freedom is discussed and corresponding quantum numbers are introduced. At the end of each section, the importance of the degree of freedom in laser cooling is explained.

2.2.1 Electronic energy levels

In general, the name of electronic energy levels are symbolically denoted as follows: a capital letter followed by ${}^{2S+1}\Lambda^{\pm}_{\Omega}$.

The capital letter denotes the electronic excitation where the ground state, first excited state, etc are denoted by X, A, B, etc. respectively. The S denotes the total electronic spin. The Λ denotes the internuclear projection of the total angular momentum J. Analogous to the angular momentum quantum number in an atom (s, p, and d), the angular momenta of a diatomic molecule are denoted by Σ, Π, and Δ. The Ω denotes the internuclear projection of the spin. The Ω is not always given because it depends on the coupling. The $\pm$ denotes the reflection symmetry of the electronic state along an arbitrary plane containing the internuclear axis [1].

As an example, consider the ground state of our laser cooling cycle: $X^2\Sigma^+_{1/2}$. This state is in the electronic ground state X, with the first excited angular momentum state Σ. The total electronic spin is 1/2 and the internuclear projection of the spin is also 1/2 [1].

In laser cooling, the main energy transition is between electronic energy levels. In our laser cooling experiment, the ground state and the excited state are $X^2\Sigma^+_{1/2}$ and $A^2\Pi_{1/2}$ respectively. The ground state is described by Hund's case (a) and the excited state is described by Hund's case (b).

Figure 2.2 shows the hyperfine levels of these two energy levels. Each hyperfine level consists of $2F + 1$ Zeeman sublevels. The ground state has a hyperfine level of $F = 2$ which contains Zeeman sublevels $m_F = -2$ and $m_F = 2$ which are not present in the excited state. This presents an issue, because a Zeeman sublevel of a groundstate can only couple to the same Zeeman sublevel in the excited state. A solution to this is discussed in Section 2.3.2.

2.2.2 Rotational energy levels

A diatomic molecule can store energy in the rotation of the atoms around each other. The quantum number for rotational energy levels is N. During an electronic energy transition, some energy can go to rotational excitations. Due to the conservation of angular momentum, some rules govern whether rotational excitations are possible, called selection rules. The selection rule is $\Delta N = 0, \pm 1$, and parity must change.

In laser cooling, it is important to use the selection rule to our advantage and limit the amount of rotational energy levels present during the laser cooling cycle. This is discussed further when the laser cooling scheme is introduced in Section 2.3.2.

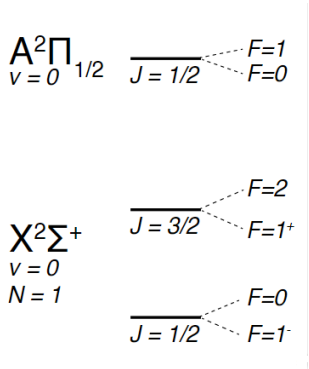

Figure 2.2: The hyperfine levels of the $J = 1/2$ and $J = 3/2$ electronic angular moment levels of the ground state and the $J = 1/2$ electronic angular moment level of the excited state of the laser cooling transition of B.

2.2.3 Vibrational energy levels

Similar to the rotational energy levels, a diatomic molecule can store energy in vibrations between the two atoms. During an electronic transition, there is a probability that some energy goes into the vibrational degree of freedom.

The likelihood this occurs depends on the overlap of the two vibrational energy levels' wavefunctions. This is denoted by Franck-Condon factors. The percentages given in Figure 2.3 are calculated based on the Franck-Condon factors given in [15]. As an example, there is a 3.4% probability of decaying to the first vibrationally excited state during the main laser cooling cycle.

2.3 Laser cooling scheme

The laser cooling scheme refers to the strategy of laser cooling. The light intensity and detuning adjust the Doppler forces to the velocity region of interest. The scattering rate of the laser cooling is maximized by limiting the amount of populated energy levels and reintroducing lost molecules to the laser cooling transition

Figure 2.3 shows a schematic of the energy levels important to our laser cooling scheme. The red arrows denote the lasers used for cooling and reintroducing vibrationally excited molecules to the cooling transition.

2.3.1 Controlling the velocity range of the Doppler force by detuning and light intensity

The detuning determines what velocities experience the largest cooling force. The detuning is adjusted in accordance to one's goals with laser cooling. This is similar to the laser intensity. Due to power broadening (defined in Section 2.4.2), the laser intensity changes the effectiveness of the laser cooling force for specific velocities. In chapter 4, two laser cooling objectives are formulated whereby the optimal laser cooling configuration is determined by simulations.

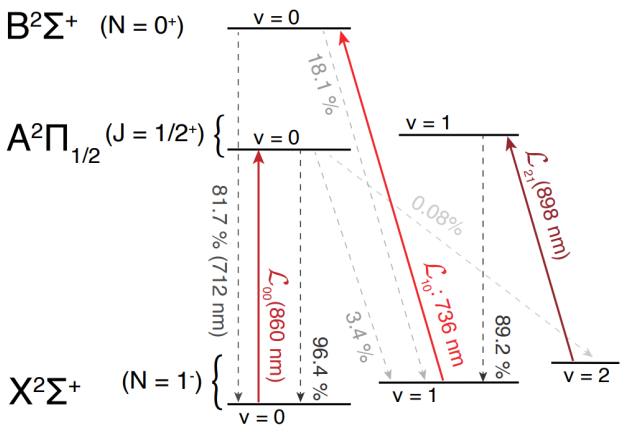

Figure 2.3: The energy levels important for our laser cooling scheme. The main laser cooling transition is between $X^2\Sigma^+(N = 1, v = 0)$ and $A^2\Pi_{1/2}(J = 1/2, v = 0)$, the 860 nm cooling laser is denoted by the dark red arrow. The other two red arrows denote the first and second vibrational repump laser. The percentages denote the branching fractions based on the Franck-Condon factors from [15]. Image made by J.W.F. van Hofslot.

2.3.2 Keeping molecules in the main cooling cycle

During laser cooling, an energy level transition is induced repeatedly. Per cycle, there is a probability that the molecule decays to a different ground state and is then lost from the cooling cycle. We discuss all possible ways the molecules can get lost from the cooling cycle and how this can be mitigated or how the molecules can be reintroduced.

Vibrational repumping

As mentioned in Section 2.2.3, each energy level transition confers a chance to enter an excited vibrational state. As seen in Figure 2.3, the probability a molecule decays to the first and second vibrationally excited state are 3.4% and 0.08% respectively.

An additional laser can pump the molecules back to the main cooling transition. For the first vibrational state, the laser is tuned such that it excites the molecules to $B^2\Sigma^+$. From thereon, 81.7% decays to the ground state of the main cooling cycle. Molecules in the second vibrationally excited state are first pumped to the first vibrationally excited state via $A^2\Pi_{1/2}(v = 1)$ state.

Given that the scattering rate is suppressed when the molecules are in a vibrationally excited state, it is paramount to reintroduce them to the cooling cycle as quickly as possible. A method to achieve this is developed in Chapter 3.

Rotational closure

As previously mentioned, it is crucial to minimize the amount of populated energy levels. One way to limit the amount of populated rotational levels is to make use of the selection rules explained in Section 2.2.2. The selection rules state that $\Delta N = 0$ or $\Delta N \pm 1$ and that parity must change. Since J is built from N the selection rule is also imposed on J.

Figure 2.4 shows one option to obtain rotation closure for the $^2\Sigma^+ \rightarrow ^2\Pi_{\frac{1}{2}}$ transition [12]. Here the blue lines indicate negative parity and the purple lines indicate positive parity. The $J' = 1/2$ can only decay to $J = 1/2$ and $J = 3/2$ in the ground state because the parity must swap.

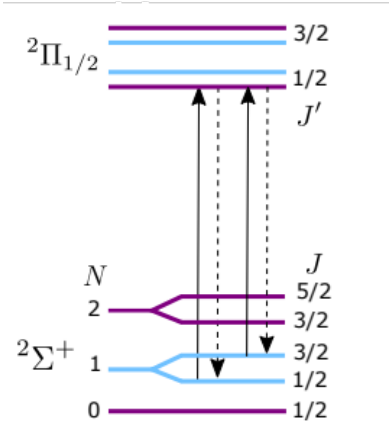

Figure 2.4: Lowest rotational energy levels of the ground state and excited state of the laser cooling transition. Purple lines have positive parity, and blue lines have negative parity. Rotational closure is obtained by driving $J = 1/2$ and $J = 3/2$ from $N = 1$ in the ground state to $J' = 1/2$ in the excited state. $J' = 1/2$ can only decay to $J = 1/2$ or $J = 3/2$ due to selection rules. The molecules can not decay to $J = 3/2$ from $N = 2$ because parity must flip. Figure from [12].

Static magnetic field for dark state remixing

It was previously shown (Section 2.2.1) that the ground state of the laser cooling transition has Zeeman sublevels that are not present in the excited state and therefore cannot be excited. These are called dark states.

A solution to this is a concept called Larmor precession. When a magnetic field is present, Larmor precession allows the Zeeman sublevels to precess into other Zeeman sublevels. The Zeeman sublevels $m_F = -2$ and $m_F = 2$ precess to $m_F = 1, 0, -1$ from where they can be excited.

In Schuman et al (2010) [22] a calculation is presented for the optimal magnetic field strength for laser cooling calcium monofluoride. Analogously, we can calculate the optimal magnetic field strength for BaF. Chapter 4 reveals this value is confirmed by simulations.

The following formula gives the Larmor precession rate for a given magnetic field,

$$\omega_B \sim B\mu_B g_F, \tag{2.1}$$

where ω_B is the Larmor precession rate, B is the size of the magnetic field, μ_B is the Bohr magnetron and g_F is Landé g factor.

Similar to Shuman et al. [22] we equate this to the linewidth of the transition, Γ. Since BaF and CaF are very similar molecules we take the same value for the Landé g factor of 1.

This gives an optimal magnetic field strength of

$$B \sim \frac{\Gamma}{\mu_B} = 2G. \tag{2.2}$$

2.4 Macroscopic aspects of the interaction between molecules and light

A molecule absorbs a photon if its energy equals the energy difference to an excited state. In this section, we discuss some macroscopic aspects of the interaction between molecules and light that are important to laser cooling.

2.4.1 Saturation intensity

The amount of photons in a light field is determined by the intensity of the light. Up to some point the laser cooling transitions are induced faster when there are more photons present. At some point, the amount of photons is no longer the limiting factor for the transition speed. This is called the saturation intensity.

It is complicated to analytically calculate the saturation intensity of BaF due to its energy level structure. For a simple two-level energy level system, the saturation intensity is calculated as follows [13],

$$I_{sat} = \frac{\pi}{r}\frac{hc\Gamma}{\lambda^3} \tag{2.3}$$

where λ is the transition frequency and Γ is the linewidth of the excited state. Using the values for our main laser cooling transition this leads to an approximated saturation intensity of 0.57 $\mathrm{mW/cm^2}$.

2.4.2 Power broadening

In essence, an energy level transition only happens if the photon has the same energy as the difference between the energy levels.

At high laser intensity, a photon can also induce the transition if its energy is slightly offset to the required energy. The higher the intensity of the light, the further the energy of the photons can be from the transition energy. This is called power broadening. It is one of the effects that cause the width of the Doppler force shown in Figure 2.1

For a theoretical explanation of power broadening see [13].

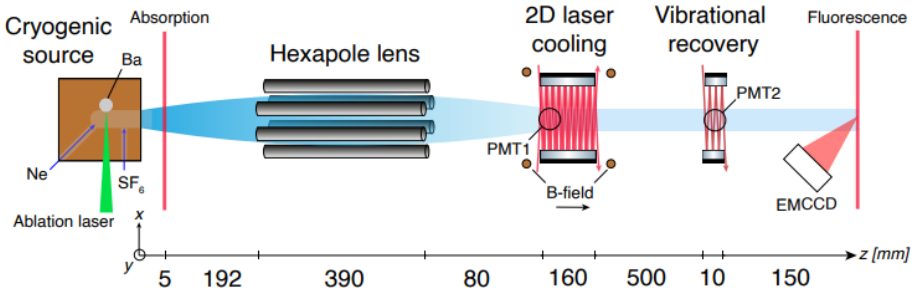

Figure 2.5: Schematic of the experimental setup for laser cooling. The blue shaded area indicates the molecular bundle. In the laser cooling section, the laser is retroreflected by two parallel mirrors to increase the interaction time. In this figure only one dimension of the laser cooling light is shown, the experiment contains another perpendicular retroreflected laser bundle. The mirrors for retroreflection are also shown in the vibrational recovery section. At the time of writing this is not yet implemented in the experiment. Image made by J.W.F. van Hofslot

2.4.3 Scattering rate for molecules

The scattering rate in laser cooling is the rate at which molecules are cycled between the ground state and the excited state of the cooling channel. One of the factors that influence the scattering rate is the lifetime of the excited state.

Another important factor that limits the scattering rate is how long the molecules spend in dark states. The longer it takes for the molecules to be pumped back to bright states the lower the scattering rate is. This is discussed in Section 2.3

The scattering rate is also suppressed by the number of energy levels that are coupled by light fields, this is due to a process called Rabi oscillations. This is the reason why the molecules in the first vibrationally excited state are reintroduced via $B^2\Sigma^+$. If they were reintroduced via $A^2\Pi_{1/2}$ this would increase the amount of energy levels coupled to the main cooling transition and reduce the scattering rate.

2.5 Experimental setup

Finally, we introduce the laser cooling experimental setup. The setup consists of a source that produces a divergent beam of BaF molecules. The molecules are then focussed by an electrostatic lens after which they travel through the laser cooling section. The laser cooling section consists of both the laser cooling light and the repump light. After the laser cooling section comes a vibrational recovery section where only repump light makes sure that all molecules are in the vibrational ground state. Lastly, the molecules are imaged by an EMCCD camera. This is shown in Figure 2.5.

Cryogenic buffer gas source

The BaF molecules are created in a cryogenic buffer gas source.

First, a solid barium target is ablated using an Nd:YAG ablation laser, creating Ba atoms. SF_6 gas is present during ablation. One of the many chemical reactions that happen is,

$$Ba + SF_6 \rightarrow BaF + SF_5, \tag{2.4}$$

creating the BaF molecule [11]. Due to the ablation of the barium target, the molecules have a high initial energy.

The cell in which BaF is created is pressurized by the ^{20}Ne buffer gas, which pushes the molecules out of the cell. The buffer gas also transfers kinetic energy from the molecules to the cell walls which cools down the molecules.

The cryogenic buffer gas source produces on the order of 10^{10} molecules per pulse per steradian and with a longitudinal velocity of ~ 190 m/s[2] and a maximum transverse velocity of ~ 5 m/s. The cell exit has a diameter of 4.5 mm. The molecules are produced at a rate of 10 Hz.

Electrostatic lens

The molecules have a large divergence when they exit the source. An electrostatic lens uses the Stark Effect, as with the Traveling-wave Stark Decelerator, to focus the molecules onto the laser cooling section. Only molecules that are low electric field-seeking are focussed by the lens [23]. This increases the amount of molecules present in the laser cooling section.

Laser cooling region

In the laser cooling region, laser beams cross the molecules multiple times in both transverse directions. The laser beams consist of light for laser cooling as well as light for repumping molecules from $X(v = 1)$ and $X(v = 2)$ states. This is discussed in more detail in Chapter 3.

A magnetic field is present to remix dark states as explained in section 2.3.2.

Above the laser cooling region is a photon multiplier tube. The PMT is used to perform frequency scans and determine transition frequencies for laser cooling and vibrational recovery.

Vibration recovery and detection region

After the laser cooling section, molecules are imaged by a photon multiplier tube (PMT) and an electron-multiplying CCD (EMCCD) camera. Prior to this, there is an extra laser beam which consists of the vibrational recovery frequencies. This ensures that all molecules are in the vibrational ground state before being imaged.

In the vibrational recovery section of Figure 2.5 there are mirrors to increase the interaction time of the vibrational recovery lasers and molecules. The current experimental setup does not include these mirrors. These might be added to the setup in the future.

3. Vibrational repumping, addressing the hyperfine levels

The energy level structure of a diatomic molecule introduces many challenges for laser cooling. The vibrational degree of freedom in a diatomic molecule allows for a molecule to go to a vibrationally excited state during an electronic transition. Such a vibrationally excited state has a different transition frequency to excite it, so once a molecule is in a vibrationally excited state it is lost from the laser cooling cycle. From the excited state of the main laser cooling transition, there is a 3.4% probability to decay to the first vibrationally excited state $X^2\Sigma^+_{1/2}(v = 1)$, previously shown in Figure 2.3. After only 100 cycles 95% of the population is in the first vibrationally excited state. As mentioned before we need on the order of 2000 cycles, so the vibrationally excited states pose a problem.

A solution to this is called vibrational repumping. In vibrational repumping, the molecules are reintroduced to the laser cooling transition by an extra laser. The vibrational repumpers in our experiment were already shown as red arrows in Figure 2.3. For the first vibrationally excited state, the molecules are excited to the $B^2\Sigma^+(N = 0, v = 0)$ from where 81.7% decay to the $X^2\Sigma^+_{1/2}$. The other molecules decay back to the first vibrationally excited state, from where the repump laser excites them again. The second vibrationally excited state is pumped to the first vibrationally excited state via $A^2\Pi_{1/2}(v = 1)$.

While the molecules are in a vibrationally excited state they are not cycled in the laser cooling transition, therefore they suppress the cooling force. It is crucial to reintroduce them to the laser cooling transition as quickly as possible.

Both vibrationally excited states have four hyperfine levels, each of which is populated during laser cooling. The experimental challenge for vibrational repumping is addressing each hyperfine level.

In this section, we develop a method to address each hyperfine level. First, we use spectroscopy to determine the spacing between the hyperfine levels. Then we add sidebands to the repumping laser by use of an electro-optic modulator (EOM). We discuss how an EOM works and present the setup that powers the EOM. From this, we find that two parameters determine the sideband layout of the EOM. These are optimized for the hyperfine structure of the vibrational excited states. The optimization is done by measuring the laser-induced fluorescence (LIF) for different EOM configurations, more LIF means that the sidebands better overlap with the hyperfine levels.

3.1 Resolving hyperfine levels of the first vibrationally excited state

In this section, we use spectroscopy to determine the spacing between the hyperfine levels of the $X^2\Sigma^+_{1/2}(v = 1)$ state. From this, we can develop a method to address each hyperfine

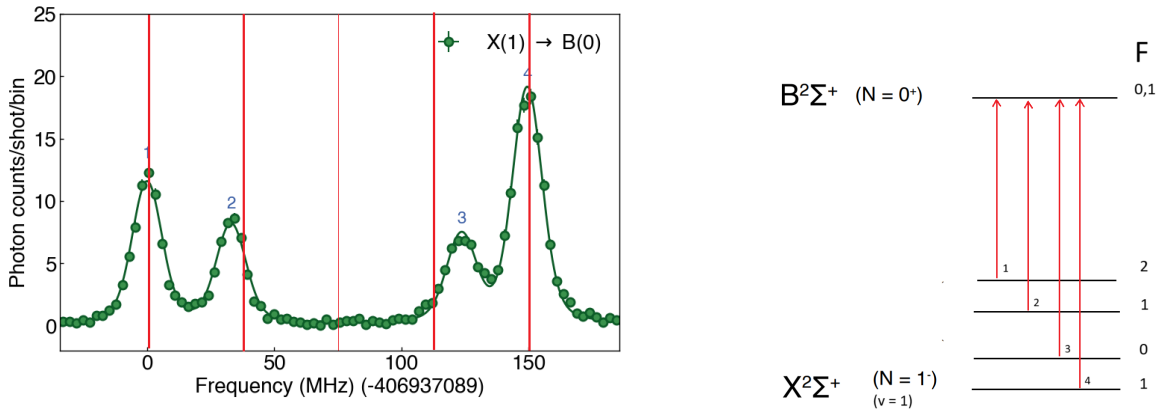

(a) **(b)**

Figure 3.1: (a) Spectroscopy showing the transitions between hyperfine levels of $X^2\Sigma^+(v = 1) \rightarrow B^2\Sigma^+(N = 0, v = 0)$. The green dots show experimental data and the green line is a fit. Peaks are at 0 ± 0.11 MHz, 33.05 ± 0.15 MHz , 123.64 ± 0.18 MHz, and 149.51 ± 0.07 MHz. The red vertical lines indicate frequencies of a laser beam at 75 MHz with first and second-order sidebands generated by an EOM driven at 38 MHz. (b) Energy level scheme for the hyperfine levels of transition of the first vibrational repumper. The small numbers next to the red lines correspond to the blue numbers in the Figure (a).

level. For now, we assume that the second vibrationally excited state has a similar hyperfine structure.

A 736 nm laser crosses the molecules in the vibrational recovery region, previously shown in Figure 2.5. The laser excites the molecules from $X^2\Sigma^+_{1/2}(v = 1)$ to the $B^2\Sigma^+(v = 0)$ state. From here the molecules decay to the $X^2\Sigma^+(v = 1)$ and emit a photon with a wavelength of 712nm. This laser-induced fluorescence is detected by the photon multiplier tube (PMT) hanging above the vibrational recovery section. By scanning the laser over a frequency range and recording the signal on the PMT the hyperfine structure of the $X^2\Sigma^+_{1/2}(v = 1)$ state is exposed.

The population is deliberately pumped into the $X^2\Sigma^+_{1/2}(v = 1)$ state to increase the signal. This is done by a laser that crosses the molecules in the laser cooling region and is tuned to excite the molecules from $X^2\Sigma^+_{1/2}(v = 0)$ to $A^2\Pi_{1/2}(v = 1)$, form here 89.2% decays to the $X^2\Sigma^+_{1/2}(v = 1)$.

The result of the spectroscopy is shown in Figure 3.1. The frequency is offset such that the first peak is at 0 MHz. In this figure, the four hyperfine levels of the $X^2\Sigma^+_{1/2}(v = 1)$ are visible by the large peaks in the photon counts. The results are fitted to determine the location of the peaks. The fit shows that the hyperfine levels are located at 0 ± 0.11 MHz, 33.05 ± 0.15 MHz, 123.64 ± 0.18 MHz, and 149.51 ± 0.07 MHz. The hyperfine levels of the excited state are unresolved.

3.2 Adding sidebands to address hyperfine levels

In this section we address the hyperfine levels of the vibrational excited states. For this, we use an optical modulator. An optical modulator can change the frequency of a light beam. The two most used optical modulators are the acousto-optic modulator and the electro-optic modulator.

An acousto-optic modulator (AOM) shifts the frequency of the light. An AOM is driven by a radio frequency signal, this signal determines frequency shift. One way to address each hyperfine level is to use four different AOMs, each specifically targeted at one hyperfine level. The advantage is that the hyperfine levels can be targeted precisely, the disadvantage is that results in a a complex and expensive setup. Such a system of four AOMs is used in the experiment to target the hyperfine transitions in the main laser cooling cycle.

An electro-optic modulator (EOM) generates multiple sidebands symmetrically around a carrier frequency, with which it can address multiple hyperfine levels. In the previous section, we found that the spacing between hyperfine levels is 0 MHz, 33.05 MHz, 123.64 MHz, and 149.51 MHz. With a carrier frequency of 75 MHz and driving frequency of 38 MHz, an EOM can generate first and second-order sidebands at -1 MHz, 37 MHz, 113 MHz and 151 MHz. Due to power broadening this allows the sidebands to overlap with the hyperfine levels.

3.2.1 An electro-optic modulator

An EOM consists of a crystal with a refractive index that is dependent on a local electric field strength. The crystal is placed between a parallel plate capacitor that controls the local electric field. The speed of light through the crystal depends on the refractive index it's refractive index, while the phase of the outgoing laser beam depends on the amount of time that the light spends in the crystal. Thus, the phase of the outgoing laser beam can be controlled by the potential on the parallel plate capacitor.

This can generate sidebands around the carrier frequency as follows. Consider a laser beam with amplitude A, frequency ω. The EOM adds a phase ϕ,

$$Ae^{i\omega t} \xrightarrow{\text{EOM on}} Ae^{i\omega t+\phi}.$$

Consider a sinusoidal phase with frequency Ω and small amplitude β such that,

$$Ae^{i\omega t+\phi} = Ae^{i\omega t+i\beta\sin(\Omega t)}. \tag{3.1}$$

When taking $\beta << 1$, a first-order Taylor expansion shows the following.

$$\begin{aligned} Ae^{i\omega t+i\beta\sin\Omega t} &\approx Ae^{i\omega t}\left(1+i\beta\sin(\Omega t)\right) \\ = A\left(e^{i\omega t}+\frac{\beta}{2}\left(e^{i\Omega t}-e^{-i\Omega t}\right)\right) &= A\left(e^{i\omega t}+\frac{\beta}{2}e^{i(\omega+\Omega)t}-\frac{\beta}{2}e^{i(\omega-\Omega)t}\right) \end{aligned} \tag{3.2}$$

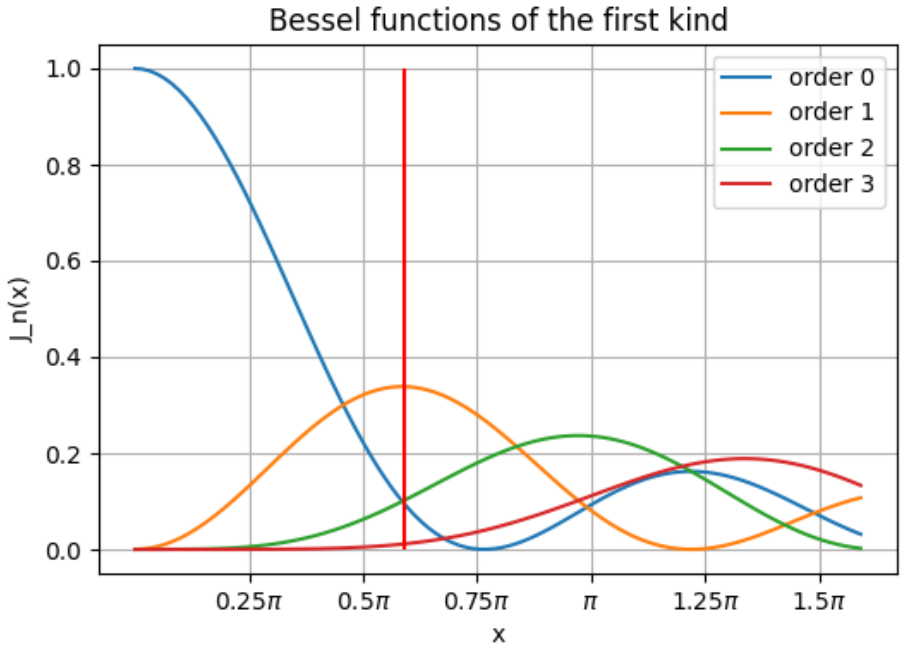

Figure 3.2: The first four order Bessel functions. Each order Bessel function represents the intensity in that order sideband. For a modulation dept of 0.6π, highlighted by the red line, 10% of the power of the laser is in the zeroth and second-order sideband while about 35% is in the first-order sideband.

For illustration purposes, one can take a first-order approximation. This shows that two extra frequency components $\omega - \Omega$ and $\omega + \Omega$ are created.

The exact result can be calculated using the following identity,

$$e^{ix\sin\phi} = \sum_{k=-\infty}^{\infty} i^k J_k(x) e^{ik\phi}, \tag{3.3}$$

with $J_k(\beta)$ being the *Bessel function of the first kind*.

With this the relation becomes,

$$Ae^{i\omega t + i\beta\sin(\Omega t)} = Ae^{i\omega t}\left(\sum_{k=-\infty}^{\infty} i^k J_k(\beta) e^{ik\phi}\right). \tag{3.4}$$

Here the Bessel function of order k determines the intensity in the k-th order sideband created by the EOM.

Figure 3.2 shows the first four orders of the Bessel function. The vertical red line highlight a modulation depth of 0.6π. Here about 10% of the power of the laser is in the zeroth and second-order sideband and about 35% is in the first-order sideband.

So in conclusion, an EOM generates sidebands symmetric around the carrier frequency. A radio frequency signal drives the EOM, this frequency determines the offset of the sidebands.

The power of the radio frequency determines the modulation depth of the EOM, which in turn determines how the light intensity is distributed over the sidebands.

3.3 Optimizing sidebands to address hyperfine levels

In this section, we optimize the driving frequency of the EOM and the modulation depth. First, we discuss the radio frequency setup that powers the EOM, then we use laser-induced fluorescence measurements to find the optimal settings.

3.3.1 Driving the electro-optic modulator

The electro-optical modulator is driven by a radio frequency (RF) signal generator. The maximum output power of this device is 20 dBm.

We calculate the required power to modulate most of the power to the first and second-order sideband. The EOM has a half wave voltage of 15 V [7], this means that 15 V results in a modulation depth of π. The impedance of the EOM is 50 Ω. This tells us that to reach a modulation depth of π we need a power output of 27.5 dBm power. We conclude that an amplifier is needed to increase the maximum output of the signal generator.

The setup shown in Figure 3.3 powers two EOMs for both vibrationally excited states. The EOM denoted by L_{10} or 735 nm is for the first vibrational state and the EOM denoted by L_{21} or 898 nm is for the second vibrationally excited state. Table 3.1 shows the output power after the gain of Amplifier 1 compared to the output power of the signal generator. The output power after the gain is measured using a frequency analyzer. With this setup, the maximum modulation depth that can be achieved is 1.52. In this setup, both EOMs are connected to the same signal generator. This means that the driving frequency and the modulation depth of both EOMs are connected. A difference in modulation depth can be achieved by using a different gain, this is not studied further in this thesis.

The experiment uses a resonant EOM optimized for a 38 MHz driving frequency. This means that the half-wave voltage of 15 V is only when the EOM is driven within 5% around the resonant frequency of 38 MHz. For a driving frequency further from resonant, more power would be required to reach the same modulation. To not be affected by this we stay between 36 MHz and 40 MHz.

3.3.2 Optimize modulation depth and driving frequency

In this section, the modulation depth and driving frequency of the EOM are optimized for the first vibrational repumper. We measure the laser-induced fluorescence (LIF) from the laser with sidebands and compare the LIF between different EOM configurations. If the EOM generates sidebands that better overlap with the hyperfine levels of the $X^2\Sigma^+_{1/2}(v=1)$ we expect a higher LIF signal.

First, the $X^2\Sigma^+_{1/2}(v=1)$ is populated by a laser that induces the transition $X^2\Sigma^+_{1/2}(v=0)$ to $A^2\Pi_{1/2}(v=1)$, from where the molecules decay to $X^2\Sigma^+_{1/2}(v=1)$. Than the laser with

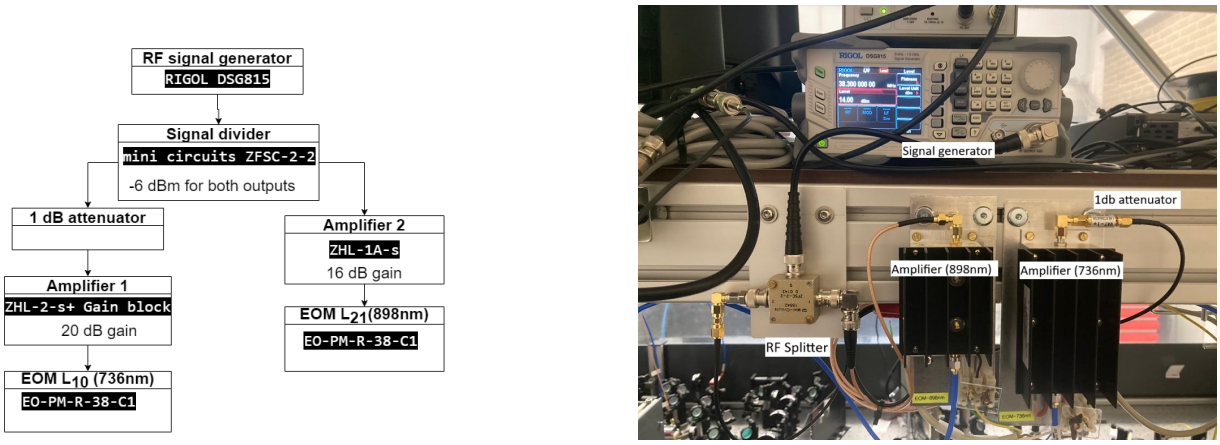

(a) **(b)**

Figure 3.3: The electro-optical modulator is powered by an RF signal generated by an amplified RF signal from a signal generator. (a) Schema of the setup, the black boxes contain the model name of the electronics. The EOM L_{10}(736 nm) is for the first repumper, and the EOM L_{21}(898 nm) is for the second repumper. (b) Picture of the setup.

Power Signal generator (dBm)	Power after gain (dBm)	Modulation depth after gain(π)
3	18.87	0.37
8	23.83	0.66
13	28.5	1.12
15	29.57	1.27
18	30.57	1.42
20	31.17	1.52

Table 3.1: A table containing measurements of the power of the RF signal after the gain of Amplifier 1. The power is measured by a frequency analyzer. The power is then converted to a modulation depth for a half-wave voltage of 15 V and an impedance of 50Ω.

sidebands induces the transition $X^2\Sigma^+_{1/2}(v=1)$ to $B^2\Sigma^+_{1/2}(v=0)$ from which the molecules decay to $X^2\Sigma^+_{1/2}(v=1)$. The photons emitted by this decay are detected by a PMT. The carrier frequency is scanned over a frequency range. Figure 3.4a shows a scan for multiple EOM configurations.

The shape of Figure 3.4 is different than the shape of the frequency scan in Section 3.1, this shows the effect of the EOM. When the carrier frequency is at the center of the plot at 75 MHz, the sidebands overlap with the hyperfine levels, similar to the situation in Figure 3.1, therefore this shows the highest peak. The smaller peaks on -40 MHz and 40 MHz are when only one of the sidebands overlaps with one hyperfine level. Figure 3.5 shows where the frequencies of the sidebands are located to create these smaller peaks.

In Figure 3.4a we see the results for different driving frequencies of the EOM. This shows that the driving frequency of the EOM affects the amount of LIF signal that results from the sideband setup.

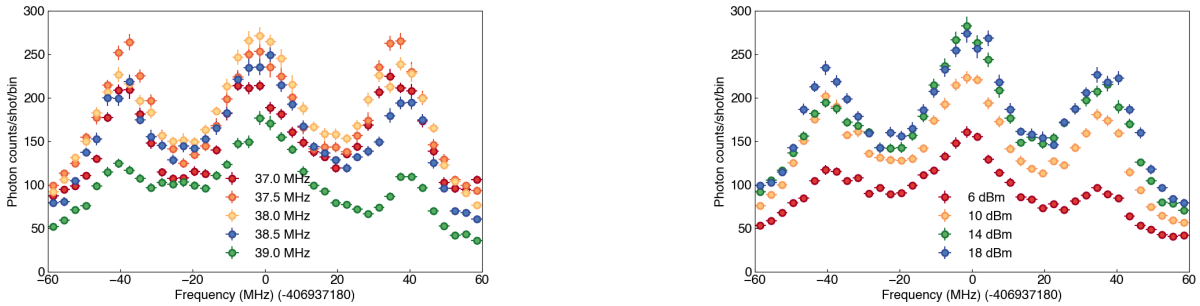

(a) **(b)**

Figure 3.4: LIF induced by a laser with EOM for a scan over carrier frequencies. (a) LIF for different driving frequencies of the EOM, the signal generator has an output power of 18 dBm (b) LIF for different signal generator output powers. The power can be converted to modulation depth using Table 3.1.

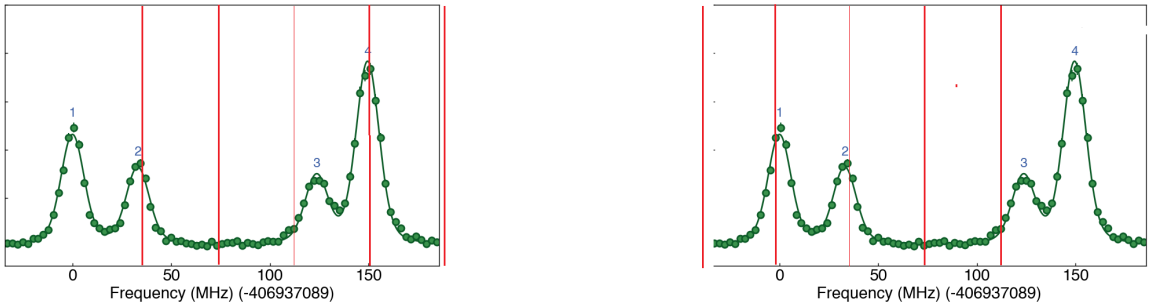

(a) **(b)**

Figure 3.5: The EOM setup that explains the two off-center peaks shown in Figure 3.4. (a) Shows the frequencies generated by the EOM that explains the peak of Figure 3.4 at about 40 MHz (b) Shows the frequencies generated by the EOM that explains the peak of Figure 3.4 at about -40 MHz

For example, a driving frequency of 39 MHz results in less LIF. When looking again at Figure 3.4a, a driving frequency of 39 MHz and a carrier frequency of 75 MHz, would result in first and second-order sidebands at -3 MHz, 36 MHz, 114 MHz, and 153 MHz. This does not overlap well with the hyperfine structure. From Figure 3.4a, we see that a driving frequency of 38 MHz results in the highest LIF signal.

Figure 3.4b shows the result for different output powers of the RF signal generator, which changes the modulation depth of the EOM. To convert the output power to a modulation depth one can use table 3.1. The LIF increases for higher modulation depth until a power of 14 dBm. Between a power of 14 dBm and 18 dBm, it does not result in a higher signal. At 18 dBm the modulation depth of 1.42. From Figure 3.2 we see that at this modulation depth, about 30% is in the first-order sideband and about 8% is in the second-order sideband.

3.4 Conclusion and Outlook

In this section, we developed a method to repump molecules from the first two vibrationally excited states to the laser cooling cycle. The modulation depth and driving frequency of the electro-optic modulator (EOM) are optimized for the first vibrationally excited state.

The symmetric spacing of the hyperfine structure is well-suited for the sidebands created by an EOM. The driving frequency and modulation depth of the EOM are optimized by analyzing the laser-induced fluorescence (LIF) that result from the overlap of the sidebands with the hyperfine levels. A higher LIF indicates better overlap with the hyperfine levels, leading to more induced transitions. We determin that a driving frequency of 38 MHz result in the most LIF. For the modulation depth, the LIF increases for deeper modulation. We determined that a modulation depth of 1.42 resulted in the most. However, the current setup limits the modulation depth that can be reached, so we did not find a maximum. This could be improved in future studies by incorporating a stronger amplifier between the signal generator and the EOM.

Another potential area for future study is the effect of light intensity on the repumper LIF. This is a possibility to improve the repumpers further.

Also, one can do an additional study on the effectiveness of the second vibrational repumper. In this study, we have optimized the EOM configuration on the first vibrational repumper and assumed this setup works for the second vibrational repumper.

4. Study on laser cooling by simulations

In a laser cooling experiment, many parameters must be optimized to obtain the desired cooling result. And, it takes time to set up a laser cooling configuration and test its outcome. Furthermore, there are only limited detection points to measure the state of the molecules.

Simulations can provide an additional method to gain insight into what happens in the experiment for a given laser cooling configuration. Also, simulations can be used to compare experimental results against.

In this chapter, simulations are used to study the effect of the detuning, light intensity, and static magnetic field on the Doppler force. We consult on an optimal laser cooling configuration for a high-velocity region and a low-velocity region, this is made more specific in the next section. We study the influence of the magnetic field and test for which magnetic field strength and angle it induces Larmor precession. Also, we study an alternative detuning strategy in which only one of the sidebands is detuned. An advantage to this is that there is no frequency component blue-detuned from a transition. At the end of this section, the simulation method is tested by reproducing a velocity-force curve of CaF 3D optical molasses previously published by Tarbutt and Devlin (2018) [3].

4.1 Formulating the laser cooling objectives

In the NL-eEDM experiment, laser cooling might be used at different locations. Therefore we formulate two velocity regions of interest in the NL-eEDM experiment.

The first objective is to reduce the transverse velocity of the molecules from 4.5 m/s, which is the maximum transverse velocity when the molecules exit the electrostatic lens, introduced in Section 2.5. This objective is referred to as Objective A. For such a laser-cooling configuration, the maximum amount of molecules coming from the lens is laser-cooled.

The second objective is to reduce the transverse velocity of the molecules to 0.25 m/s. With this velocity, the molecules stay within the radial acceptance of the interaction zone at the end of the NL-eEDM experiment. The end of the interaction zone is at a distance of about 4 m and the radial acceptance is on the order of 5 mm. To reach this the maximum transverse velocity is 0.25 m/s. This objective is referred to as Objective B.

4.2 A model of the laser cooling experiment

In this section, we explain how the laser cooling experiment is simulated. First, the mathematical model of laser cooling and implementation into Python is introduced. Then we show the implementation of our laser cooling experiment as well as the scenario that is simulated. Finally, we discuss the velocity-force curve that results from the simulation. We show how this velocity-force curve indicates the effectiveness of the laser cooling configuration for a specific velocity region.

The simulation is based on a package called PyLCP, published by Eckel et al. (2020) [5]. The package is an object-oriented program that takes a representation of the molecule, the laser beams, and a magnetic field and uses Optical Bloch Equations to calculate the laser cooling force for a specific velocity and position of the molecule.

The BaF molecule

To model the ground and excited state of the BaF, PyLCP provides a helper functions. These helper functions require a parameterization of the molecule together with the quantum numbers. As previously described in Section 2.2, our experiment uses the transition between $X^2\Sigma_{\frac{1}{2}}$ and $A^2\Pi_{\frac{1}{2}}$ for laser cooling.

Table 4.1 lists the parameters to model the BaF molecule in PyLCP.

Name	value	Source
Frosch and Foley a parameter	26.55 MHz	NL-eEDM (2022) [6]
Rotational constant for X state	0.2158 cm^{-1}	Knight et al. (1971) [17]
Rotational constant for A state	0.2118 cm^{-1}	Mohanty et al. (1970) [21]
Isotropic spin-spin interaction	63.509 MHz	Ernst et al. (1986) [10]
Anisotropic spin-spin interaction	8.224 MHz	Ernst et al. (1986) [10]
Electron-spin rotational coupling constant	80.923 MHz	Ernst et al. (1986) [10]

Table 4.1: The parameters used to model the X and A state of the BaF molecule in PyLCP.

With this parameterization PyLCP can calculate the spacing of the hyperfine energy levels, this is shown in Figure 4.1. Table 4.2 compares the experimentally measured spacing between the hyperfine energy levels to the spacing based on the energy levels of PyLCP.

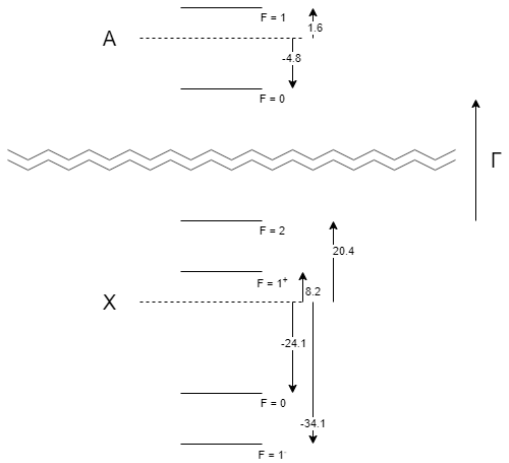

Figure 4.1: The energy levels of the ground and the excited state of BaF calculated by PyLCP in units of linewidth. The linewidth is 2.8 MHz.

transition	scan + fit (MHz)	scan + fit (Γ)	PyLCP (Γ)
$F = 2 \rightarrow F' = 1$	0 ± 0.16	0	0
$F = 1^+ \rightarrow F' = 0$	16.84 ± 0.15	6.01	5.88
$F = 1^+ \rightarrow F' = 1$	33.70 ± 0.17	12.04	12.25
$F = 0 \rightarrow F' = 1$	123.45 ± 0.18	44.09	44.55
$F = 1^- \rightarrow F' = 0$	134.89	48.18	48.20
$F = 1^- \rightarrow F' = 1$	151.74 ± 0.07	54.20	54.56

Table 4.2: A comparison of the energy levels calculated by PyLCP to the transitions measured experimental data. The transition frequencies are taken relative to $F = 2 \rightarrow F' = 1$. The values in the last column are calculated based on the values of Figure 4.1.

The laser beams

Figure 4.2a shows the laser cooling setup in the simulations. The red arrows indicate the laser beams, the green arrow is the homogeneous magnetic field, and the blue arrow is the molecules' velocity. The light is linearly polarized in the z-direction of Figure 4.2a.

In PyLCP, the light intensity is specified in units of saturation intensity. For the saturation intensity PyLCP assumes a two-level system, previously determined in Section 2.4.1 to be 0.57 mW/cm^2. To calculate the laser intensity one multiplies the saturation times the saturation intensity of 0.57 mW/cm^2.

To compare the simulated intensity to the laser power in the experiment one can calculate the laser power for a Gaussian-shaped laser beam. The peak of the Gaussian shape is the laser intensity at the center of the laser beam. Using the following formula,

$$V = \frac{A\pi w^2}{4}, \tag{4.1}$$

where A is the amplitude of the Gaussian and w is the $1/e^2$ radius of the beam. As an example, a laser beam with a saturation parameter of 1 for a $1/e^2$ radius of 10 mm has a total power of 4.5 mW. For the comparison to the experiment, note that in the simulations the molecule constantly experiences the maximum intensity, whilst in the experiment the molecule flies through the Gaussian-shaped beam and experiences a changing intensity. Later in this section, we convert the saturation to laser power for a Gaussian beam with a $1/e^2$ radius of 10 mm.

Each simulated laser beam consists of four frequency components to target each hyperfine transition. The transitions targeted in the simulations are,

$$\begin{aligned}(F = 2 \rightarrow F' = 1) + \delta \\ (F = 1+ \rightarrow F' = 0) + \delta \\ (F = 0 \rightarrow F' = 1) + \delta \\ (F = 2- \rightarrow F' = 1) + \delta,\end{aligned}$$

where δ is the detuning. Figure 4.2b shows the frequency scan of the $X^2\Sigma_{\frac{1}{2}} \rightarrow A^2\Pi_{\frac{1}{2}}$ transition together with laser beam frequencies. This is the same as the current laser cooling scheme in the experiment, stated in Section 2.3.

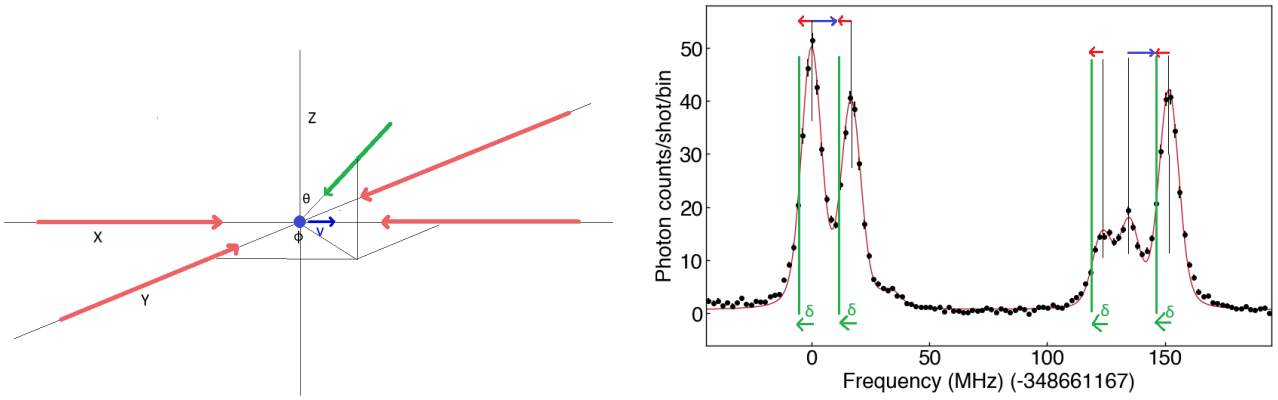

(a) **(b)**

Figure 4.2: Setup in the laser cooling simulations (a) Particle, given in blue, has a velocity in x-direction. Four lasers, the red arrow, interact with the particle to induce laser cooling. The magnetic field, given by the green arrow, induces Larmor precession for dark state remixing. (b) A frequency scan exposing the hyperfine structure of the $X^2\Sigma_{\frac{1}{2}} \rightarrow A^2\Pi_{\frac{1}{2}}$ transition. The green lines indicate the frequencies of the laser cooling light beam. The red arrows on the top indicate the red-detuning causing laser cooling. The blue arrows on the top indicate blue-detuning which can cause Doppler heating at high light intensity.

This frequency setup has one disadvantage. From Figure 4.2b we see that some laser frequencies are not only red-detuned from a transition on the right of the frequency but also blue-detuned from a transition on the left. Earlier we found that, when a frequency is blue-detuned from a transition this causes Doppler heating. This is highlighted by the red and blue arrows in Figure 4.2b. In Section 4.5 we study the effectiveness of an alternative detuning strategy where this problem is mitigated.

Caveat: No vibrationally excited states simulated

These simulations do not include vibrationally excited states. With vibrationally excited states, the scattering rate is reduced which results in a lower Doppler force. This can be accounted for by reducing the results in this section by a constant factor.

For an example of an appropriate reduction due to the vibrationally excited state, one can look at the article by J.A. Devlin and M.R. Tarbutt (2018) [3]. They reduce their force functions between 16% and 65% to account for vibrationally excited states. They base these numbers on a simulation where they include the vibrationally excited state. In the future, it would be insightful to research such reduction factors for our laser cooling simulations.

4.2.1 The result of a simulation: the velocity-force curve

The simulation computes a force for a given velocity of the particle. A range of velocities generates a velocity-force curve, previously introduced in Section 2.1.1. In this chapter, the force is converted to acceleration for intuitive interpretation.

From a velocity-force curve, one can determine the effectiveness of the velocity-force curve for

a certain velocity range. To quantify the effectiveness, one can look at the integral of the velocity-force curve between two velocities. This value tells something about the amount of energy lost due to the velocity-force curve. A larger area means less time from one velocity to the other.

With the velocity-force curve, one can calculate the time required to go from one velocity to another for a given velocity-force curve. The following derivation,

$$\begin{aligned} a &= f(v) \\ \frac{\mathrm{d}v}{\mathrm{d}t} &= f(v) \\ \int \frac{dv}{f(v)} &= \Delta t, \end{aligned}$$

where the acceleration is equated to a general function of velocity, $f(v)$ shows that the interaction time is obtained by integrating the inverse of the velocity-force curve.

With a specified interaction time and the enter velocity, the velocity with which the molecule exits the laser cooling section can be calculated. Similarly, with a specified interaction time and velocity with which the molecule exits the laser cooling section, the required entry velocity can be calculated.

These analysis methods are used to quantify the quality of a velocity-force curve.

4.2.2 Codebase

The codebase developed for this work contains three classes of files, divided into directories. The first directory, called model, contains all files responsible for modeling the experiment. In this directory, there is a specific file for the Hamiltonian, laser beams, magnetic field, and molecules. The second directory, called execution, is responsible for executing the simulations and saving and loading the data. The third directory, called analysis, contains all the code required for the analysis of the results.

The codebase can be found on the Gitlab of the NL-eEDM group, readme files are provided for guidance through the files.

A typical velocity-force curve, consisting of 30 points, takes about 4 hours to run on 32 GB RAM. To run many simulations simultaneously, we have used the supercomputer of the University of Groningen.

4.3 Optimization of laser cooling configuration

This section presents a study on the optimal detuning, light intensity, and magnetic field strength for our two laser cooling objectives stated in Section 4.1. The first objective is to reduce the transverse velocity of the molecules from an entry velocity of 4.5 m/s. The second objective is to reduce the transverse velocity of the molecules to an exit velocity if 0.25 m/s. We simulate different laser cooling configurations and compare the velocity-force curve. Table

4.3 lists the simulated parameters in this section. In total this results in 648 velocity-force curves.

Description (Unit)	Range (Stepsize)	Amount
Saturation (1)	2 ↔ 15 (0.5)	27
Detuning (Γ)	-0,5 ↔ -2 (0.5)	4
Mag field strength (G)	0.5 ↔ 3 (0.5)	6

Table 4.3: Simulation parameters used in this section, within these ranges we look for an optimal laser cooling configuration for the two laser cooling objectives. In total there are 648 configurations.

Figure 4.3 shows a handful of velocity-force curves for detunings, saturations, and magnetic field strengths throughout the ranges earlier specified. This shows the effect of each parameter on the velocity-force curve. Each row of Figure 4.3 shows the result with a different detuning and each column shows the result with a different magnetic field strength. Each plot contains the velocity-force curve of three different saturations. The vertical purple line denotes the velocity at which the molecule's velocity exactly cancels the detuning of the light.

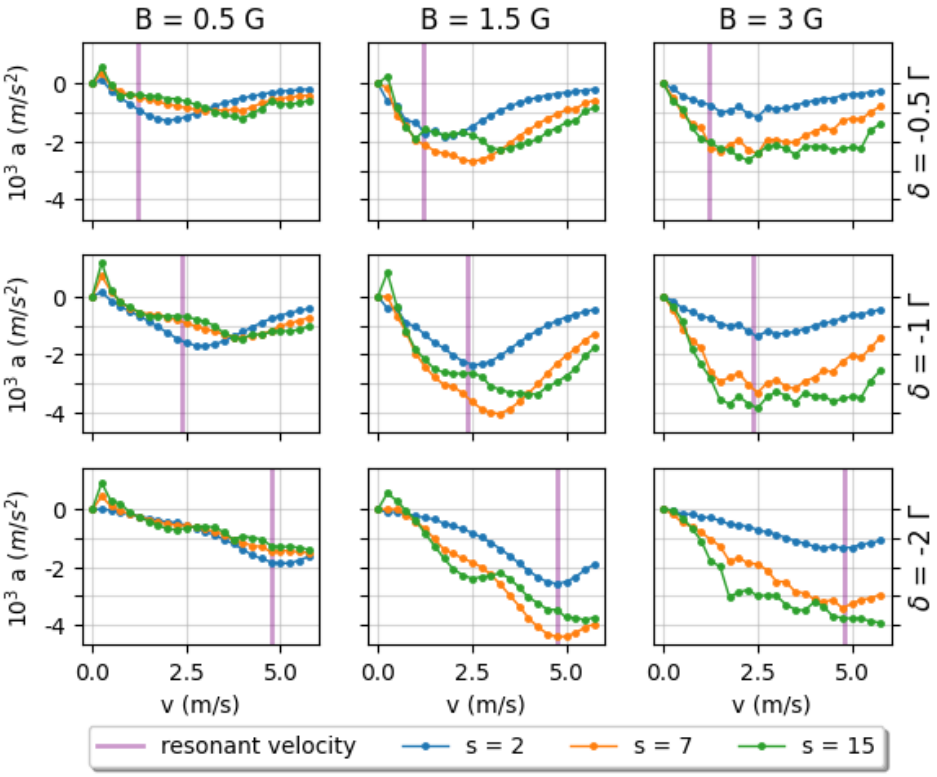

Figure 4.3: A small sample of velocity-force curves to show the effect of detuning, light intensity, and magnetic field on the Doppler force. Configurations shown are: detunings(Γ) -0.5; -1; -2, saturations 2; 7; 15, and magnetic field strengths (G) 0.5; 1.5; 3. The purple line denotes the resonant velocity.

In the first row, with a detuning of -1 Γ, the Doppler force peaks at around 2.5 m/s which is

a higher velocity than the resonant velocity. This effect is best visible for higher saturations. For higher detunings, the Doppler force does peak at resonant velocity.

For a magnetic field of $B = 0.5$ G the Doppler force is highly suppressed, this is because the Larmor precession rate is much lower than the linewidth. So the molecules spend a long time in dark Zeeman sublevels. At $B = 1.5$ G the Doppler force is more than double in strength. The velocity-force curve is smoothest for a magnetic field strength of $B = 1.5$ G and the Doppler force has a narrow peak around resonant velocity. At magnetic field $B = 3$ G the velocity-force curve has similar strength as $B = 1.5$ G but the peak at resonant velocity is much wider. Also, the velocity-force curve is less smooth.

4.3.1 Effectiveness of a velocity-force curve

In this section, we consider all 648 configurations. We quantify the effectiveness of the velocity-force curve by looking at the area under the curve for the two earlier specified velocity regions. Finally, the entry and exit velocities are calculated for the provided interaction time.

In this section, each result only includes a subset of the full configuration space. In general, the configurations shown in this section are the configurations with the highest area under the curve together with the configurations besides this optimum. In Appendix A.1 the results containing all configurations are shown.

Figure 4.4 shows the area under the velocity-force curve between velocities 3.5 m/s and 4.5 m/s. This shows us how effective the configuration is for the velocity range interesting for Objective A. The lower boundary 3.5 m/s is arbitrarily chosen, later this is chosen more specifically when we include the interaction time.

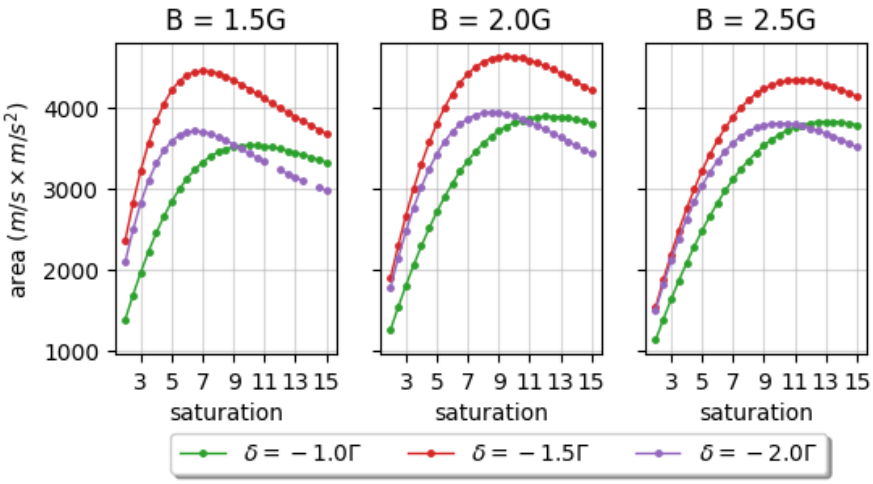

Figure 4.4: The area under the velocity-force curve between 3.5 m/s and 4.5 m/s, each plot is for a different magnetic field strength. Each plot shows the result for three different detunings. Only the configurations are shown that result in the highest area. See Figure A.1 for all configurations.

Figure 4.4 shows that a detuning of $-1.5\ \Gamma$ is most effective for cooling a molecule from 4.5 m/s.

Generally, a detuning of $-1\ \Gamma$ or $-2\ \Gamma$ has about 5% to 15% less area under the curve.

The most effective magnetic field is $B = 2$ G, but the magnetic field $B = 1.5$ G and $B = 2.5$ G only about 5% less area under the curve. The effect of the magnetic field is studied more carefully in the next section. Interestingly from the figure, we see that when a larger magnetic field strength is used, the area under the curve is largest for higher saturation.

For the saturation, with a magnetic field of $B = 2$ G the area under the curve is largest between 7 and 11 times saturated, this would translate to a power between 31.5 mW and 49.5 mW following the conversion presented in Section 4.2. The area under the curve reduces quicker for situations below optimal than for saturation above optimal. This shows that for larger light intensity the power broadening causes Doppler heating in the transition that is blue-detuned by two of the sidebands.

Figure 4.5 shows the area under the velocity-force curve between the velocities 0.25 m/s and 1 m/s. This shows the effectiveness of the curves for a velocity range interesting for objective B. Again the upper bound of 1 m/s is chosen arbitrarily.

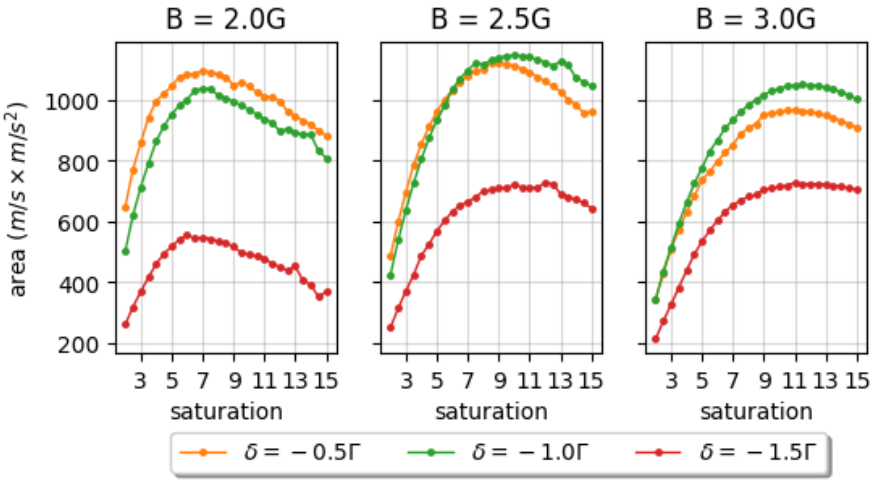

Figure 4.5: Area under the velocity-force curve between 0.25 m/s and 1 m/s, each plot is for a different magnetic field strength. Each plot contains the result for three different detunings. Only configurations shown have the largest area under the curve, see Figure A.2 for all configurations.

From Figure 4.5 we see that for objective B a lower detuning is required. For this velocity region, there is almost no difference between $-0.5\ \Gamma$ and $-1\ \Gamma$. This corresponds to what we already saw in Figure 4.3. For a detuning of $-0.5\ \Gamma$, the peak of Doppler force remained at a velocity higher than resonant velocity.

The magnetic field shows a similar effect as in Figure 4.4. The highest area is for a magnetic field of 2.5 G but with only a small improvement to the magnetic fields 2 G or 3 G.

In Figure 4.4 the area under the velocity-force curve is around 4000 $m/s \times m/s^2$ while in Figure 4.5 the area is a factor four lower. This shows that Doppler cooling can extract more energy in the velocity region of objective A than in the velocity region of objective B.

4.3.2 Entry and exit speed for the velocity-force curve

When the interaction time of the laser cooling section is known, a velocity-force curve allows us to calculate the entry or exit velocity given an exit or entry velocity respectively. The interaction time is taken as 0.8 ms.

Figure 4.6 shows what exit velocity can be reached within the interaction of 0.8 ms for an entry velocity of 4.5 m/s. This shows how much the transverse velocity of the molecules can be reduced for objective A. The blue line highlights the entry velocity of 4.5 m/s.

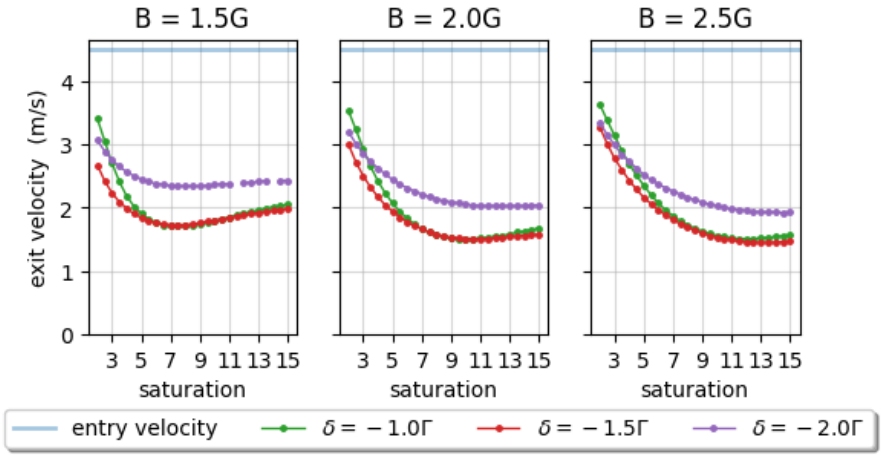

Figure 4.6: The exit velocity to which the transverse velocity of a molecule can be reduced when it enters the cooling section with a velocity of 4.5 m/s. Only configurations are shown where the exit speed is lowest, for all configurations see Figure A.3.

Figure 4.6 shows that we can cool molecules from 4.5 m/s to about 1.5 m/s. This can be reached for a detuning of -1.5 Γ. The light intensity must be above 6 times saturated. The trends over the different configurations are similar to what was already shown in Figure 4.4. This plot shows that the velocity that can be reached is nearly identical for magnetic fields between 1.5 G and 2.5 G.

Figure 4.7 shows the maximum entry velocity such that the transverse velocity can be reduced to an exit velocity of 0.25 m/s within the interaction of 0.8 ms. The blue horizontal line highlights the exit velocity. For some configurations, no data point is shown in Figure 4.7, this means that for this configuration the transverse velocity of the molecule cannot be reduced to 0.25 m/s because at low velocities the sub-Doppler force has positive acceleration on the molecules, examples of this where shown in Figure 4.3.

In Figure 4.7 we see a larger influence of the magnetic field strength than what was visible in Figure 4.5. This is due to sub-Doppler forces appearing at low velocities. If the sub-Doppler forces cause positive acceleration at 0.25 m/s, this velocity can not be reached. While this is not shown by looking only at the area under the curve. But even when the sub-Doppler force does not cause a positive acceleration it can highly suppress the negative acceleration of the Doppler force. This effect is more evident when calculating the velocity that is reached within the interaction time. From this, we can learn that the magnetic field is more important when

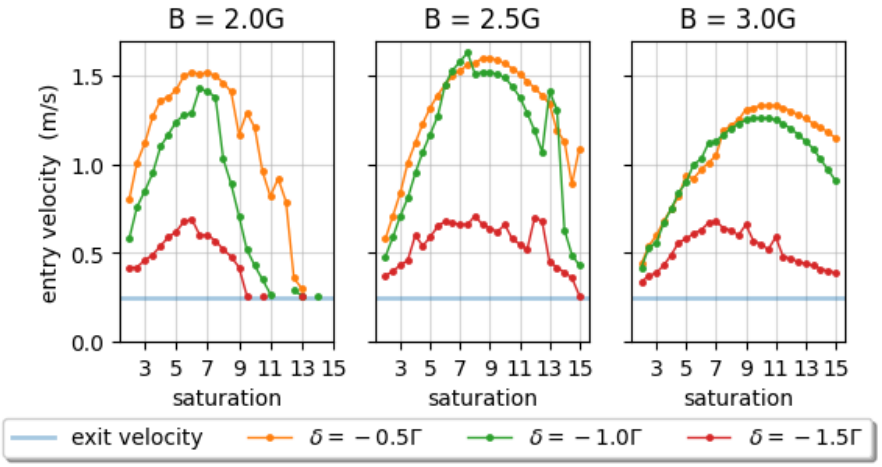

Figure 4.7: The entry velocity to which the transverse velocity of a molecule can be reduced when it enters the laser cooling region with a velocity of 0.25 m/s. Only configurations are shown with the highest entry velocity, for all configurations see Figure A.4.

Doppler cooling in the low-velocity region.

4.4 Static magnetic field influence on laser cooling

In this section, we study the effect of the magnetic field strength and the angle between the magnetic field and the polarization of the light on the Doppler cooling force.

In Section 2.3.2 we discussed the existence of dark Zeeman sublevels due to the type-II laser cooling scheme. We found that a static magnetic field gives rise to Larmor precession which rotates the dark Zeeman sublevels to bright Zeeman sublevels. The magnetic field strength determines the Larmor precession rate and thus influences how long a molecule is in a dark Zeeman sublevel. A molecule in a dark Zeeman sublevel suppresses the scattering rate of the laser cooling transition and lowers the Doppler cooling force. Earlier we found that the theoretical optimal magnetic field strength is 2 G

For the Larmor precession, the magnetic field must be at a certain angle to the quantization axis of the molecule. The polarization of the laser light determines the quantization axis. Thus the angle between the magnetic field and the polarization of the light affects the Larmor precession [24].

In the previous section, we already saw the effect of the magnetic field on the Doppler forces. In this section, we study this more precisely. The angle is defined such that at 0 °, the magnetic field is parallel to the polarization of the light, at 90 ° it is perpendicular, and at 180 ° it is anti-parallel to the light polarization.

In this section, we only change the magnetic field. Each simulation is run with a saturation of 10 and a detuning of -1.5 Γ.

4.4.1 Results

From Figure 4.8 we see the influence of the magnetic field on the laser cooling force curve. The plot on the left shows velocity-force curves for different magnetic field strengths. The angle between the magnetic field and light polarization is constant at 45 °. We see that for a magnetic field strength of 0.2 G the Doppler force is suppressed, which hints at a dark state remixing that is too slow. This causes the Doppler force to be a factor 10 lower than for a magnetic field of 2 G. For a magnetic field of 4 G the Doppler force is also suppressed compared to the Doppler force at a magnetic field of 2 G.

We see a sub-Doppler force appearing at low magnetic field strengths of 0.2 G and 1 G for low velocities. The transverse velocity of a molecule cannot be reduced to a velocity where there is positive acceleration.

In the right plot of Figure 4.8, one can see the effect of the angle between the magnetic field and polarization. For low angle, where the magnetic field is near perpendicular to the light polarization, here the magnetic field cannot cause Larmor precession. This suppresses the Doppler force. The Doppler force has similar strength between 30 ° and 60 °.

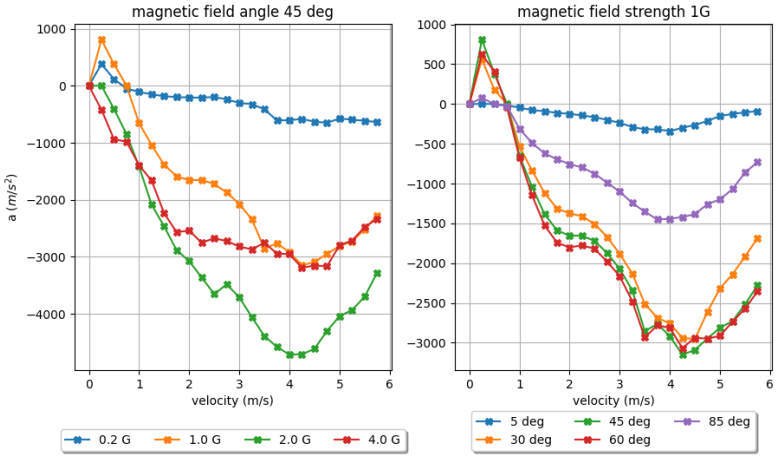

Figure 4.8: The velocity-force curves for different magnetic fields. This shows the effect of the magnetic field strength and angle on the laser cooling curve. The left plot shows the result of different magnetic fields between 0.2 G and 4 G for a magnetic field angle of 45 °. The plot on the right shows the result for different magnetic field angles and magnetic field strength of 1 G.

Next, we study the effect of the magnetic field specifically on the two velocity regions stated by the laser cooling objectives of Section 4.1. We use a similar approach as in Section 4.3.

For objective A, we look at the area under the velocity-force curve between 3.5 m/s and 4.5 m/s. Also, we look at the velocity that can be reached within the interaction time of 0.8 ms and an entry velocity of 4.5 m/s. This is both shown in Figure 4.9, the area and exit velocity are shown in the same plot with different scales on the y-axis. The blue horizontal line highlights the entry velocity of 4.5 m/s. The plot on the left shows the effect of the magnetic field strength,

and the plot on the right shows the effect of the angle between the magnetic field and light polarization.

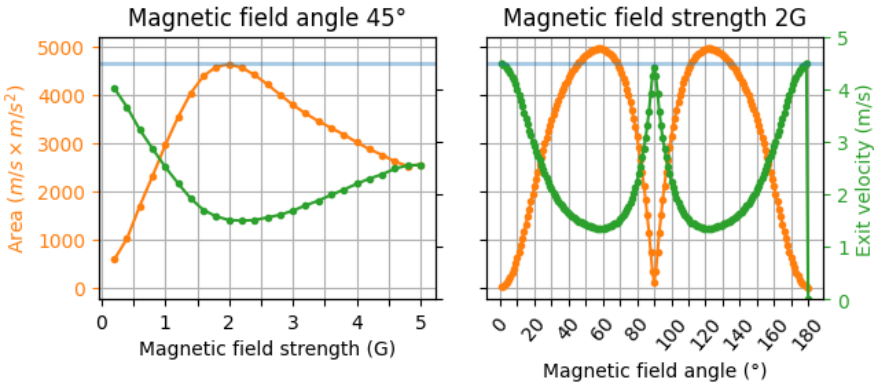

Figure 4.9: The area under the curve between 3.5 m/s and 4.5 m/s is shown by the orange line. The green line shows the velocity that can be reached with an entry velocity of 4.5 m/s. The plot on the left shows different magnetic field strengths, and the plot on the right shows different magnetic field angles.

For the magnetic field strength, we see that between 1.5 G and 2.5 G, the Doppler force is most effective for objective A. For a magnetic field below 1.5 G, the Doppler force reduces linearly until it has almost no effect. We can also see that the Doppler force for a magnetic field above 2.5 G reduces much slower than below 1.5 G. The minimum velocity to which the transverse velocity of the molecules can be reduced is 1.5 m/s at a magnetic field strength between 1.5 G and 2.5 G.

From the left plot of Figure 4.9 we see that the angle between the magnetic field and the light polarization has a large effect on the Doppler cooling force. When the magnetic field is parallel, perpendicular, or anti-parallel to the light polarization, the Doppler force completely disappears. At this point, the magnetic field cannot cause Larmor precession and remix dark states.

Between 40 ° and 60 ° or between 110 ° and 140 ° is the optimum angle between the magnetic field and light polarization. Here the Doppler force is most effective. Outside of this region the Doppler force quickly reduces to zero.

For objective B, we look at the area under the velocity-force curve between 0.25 m/s and 1 m/s. Also, we look at the maximum velocity from which it can be reduced to 0.25 m/s within the interaction time of 0.8 ms. This is shown in Figure 4.10. The blue horizontal line highlights the exit velocity of 0.25 m/s. The plot on the left shows the effect of the magnetic field strength, and the plot on the right shows the effect of the angle between the magnetic field and light polarization.

From Figure 4.10 we see for the low-velocity region of objective B, the magnetic field has a very different effect on the Doppler force than for objective A. This has to do with the sub-Doppler forces that appear at a low magnetic field. For the magnetic field strength, we see that the Doppler force is most effective for a magnetic field strength between 2.5 G and 4.5 G. Regarding

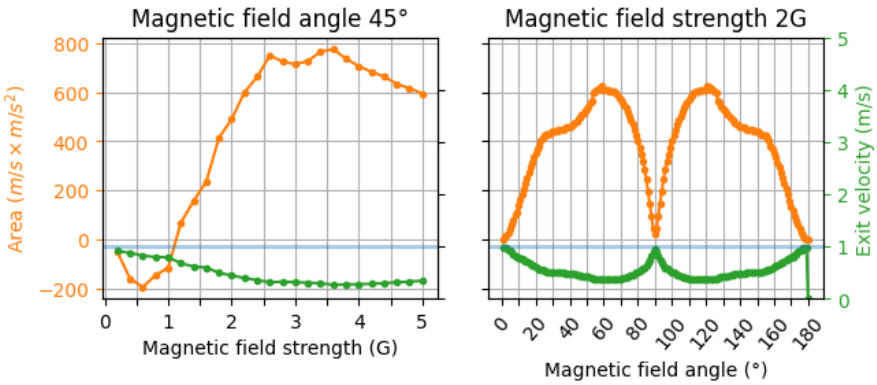

Figure 4.10: The area under the curve between 0.25 m/s and 1 m/s is shown by the orange line. The green line shows the maximum entry transverse velocity with which it can be reduced to an exit velocity of 0.25 m/s. The plot on the left shows different magnetic field strengths, and the plot on the right shows different magnetic field angles.

the angle between the magnetic field and light polarization, we see a similar effect as before. Only we see an additional bend around 45 ° and 125 °, until now it is not clear what causes this sudden drop in the area.

4.5 An alternative detuning strategy

In this section, we study the effectiveness of an alternative frequency setup. We already saw that when all sidebands are equally red-detuned from its transition, some frequencies are also blue-detuned from another transition. This can cause unwanted Doppler heating.

In this section, we only detune the sideband that targets the transition $F = 2 \rightarrow F' = 1$. This is the transition on the left of Figure 4.11. This means that only molecules in $F = 2$ contribute to the Doppler cooling force. The other three sidebands act as repumpers and pump molecules to the $F = 2$ hyperfine level. Since no sideband is blue-detuned from a transition it is possible to go to higher laser intensity intensity without causing Doppler heating due to power broadening.

In this section, we use a similar approach to Section 4.3 to research the effectiveness of this laser cooling configuration for the two laser cooling objectives. We compare the results to the standard standard setup. In this section, we only vary the light intensity of the sideband that is detuned. The other sidebands have a light intensity of 5 times saturation in each simulation.

In Figure 4.12 we see the velocity-force curves for different detuning, saturation, and magnetic field strengths using the alternative frequency setup. The first thing to notice is that at its peak the Doppler force is much lower than for the traditional frequency setup, even at 19 times saturation. Another thing to notice is that the light intensity has much less influence on the strength of the Doppler force since we are only detuned with one sideband. Another difference with the velocity-force curves of the traditional frequency setup is that the peak of the Doppler

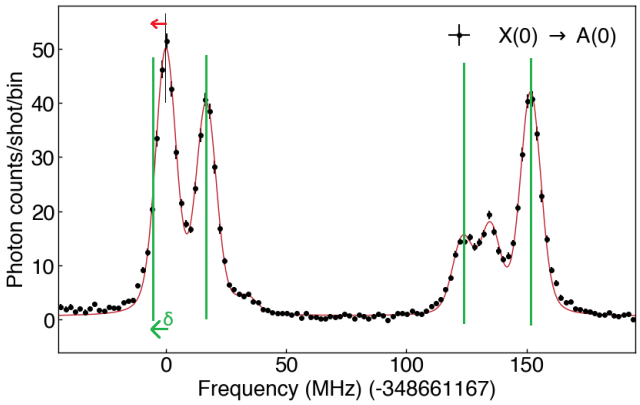

Figure 4.11: A schematic of the alternative detuning strategy, where only one of the sidebands has a detuning. A frequency scan exposing the hyperfine structure of the $X^2\Sigma_{\frac{1}{2}} \rightarrow A^2\Pi_{\frac{1}{2}}$ transition. The green lines indicate the frequencies of the laser cooling light beam. The red arrows on the top indicate the red-detuning causing laser cooling.

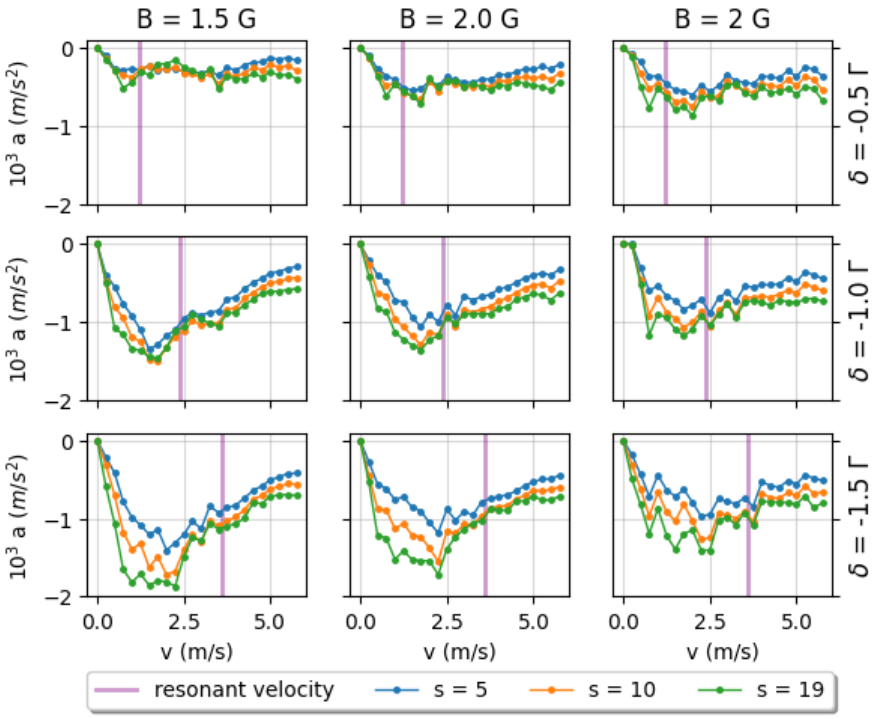

Figure 4.12: Force curves for a variety of configurations of the alternative laser cooling scheme. The saturation parameter denotes the saturation of the detuned frequency component. The resonant frequency components are always at a saturation of 5.

force is not at resonant velocity for detuning $-1.5\ \Gamma$. Such velocity-force curves would not be effective for objective A since there is no strong Doppler force around 4 m/s. It requires further research to determine why the Doppler force does not peak at resonant velocity for a detuning of $-1.5\ \Gamma$.

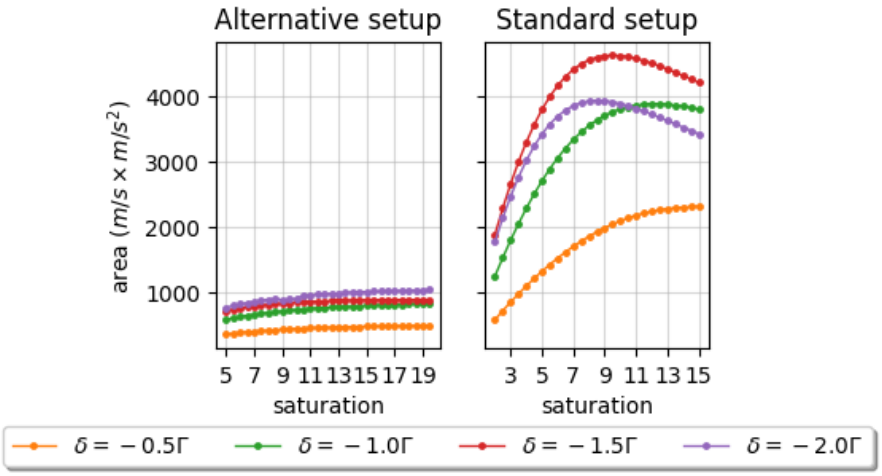

Figure 4.13: A comparison between the conventional and the alternative detuning strategy. Lines show the area under the velocity-force curve between 3.5 m/s and 4.5 m/s, for a variety of configurations for both alternative frequency setup and standard setup. The magnetic field is $2G$.

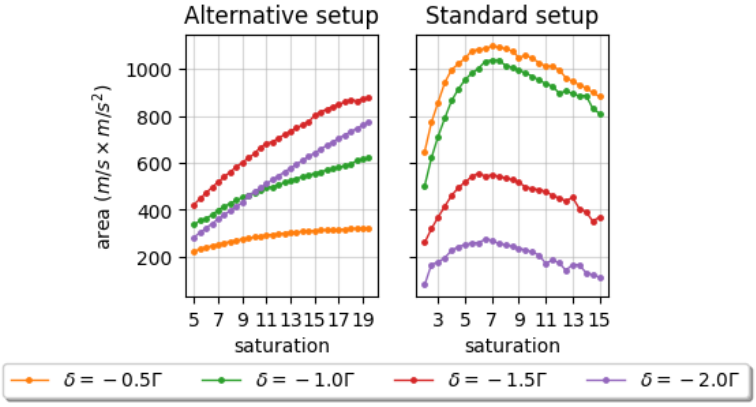

Figure 4.14: A comparison between the conventional and the alternative detuning strategy. The lines show the area under the velocity-force curve between 0.25 m/s and 1 m/s, for a variety of configurations for both alternative frequency setup and standard setup. The magnetic field strength is $2G$.

For a direct comparison between the effectiveness of the alternative frequency setup to the original setup, we look at the area under the velocity-force curve. Figure 4.13 shows the area under the velocity-force curve between 3.5 m/s and 4.5 m/s, for different detunings and a magnetic field strength of 2 G. This confirms that the alternative laser cooling setup is not effective for laser cooling object A.

For object B, Figure 4.14 shows the area under the curve between 0.25 m/s and 1 m/s compared to the traditional laser cooling setup. The alternative laser cooling is more promising in this area, but even at a light intensity of 19 times saturated, it does not yield a larger area under the curve than the traditional frequency setup. The results show that it is possible to go

to higher light intensity without Doppler heating because no sideband is blue-detuned of a transition.

4.6 Reproducing published work to test simulation setup

To test the reliability of the PyLCP package we reproduce a simulation performed by J.A. Devlin and M.R. Tarbutt (2018) [3]. Devlin and Tarbutt study the behavior of the calcium monofluoride molecule in 3-dimensional optical molasses. They use their numerical model based on multilevel Optical Bloch Equations to calculate velocity-force curves. More information on the model can be found in the article [3].

In this section, the simulations performed by Devlin and Tarbut are reproduced using our simulations. This gives an idea about the accuracy of the results of our simulations. To reproduce the results we only change the parameterization of the molecule to represent CaF, and the laser setup to reproduce the 3D molasses.

Laserbeam setup

In the simulation of Devlin and Tarbutt, they use frequency components addressing the four hyperfine levels in the ground state. The 3D optical molasses consists of six laser beams, pointing in both directions of the three dimensions. Each frequency component has a circular polarization, three of them are minus polarized and the component addressing $F = 1^+$ ground state has plus polarized light, see Figure 1b of [3]. Each simulation has the same detuning of -0.64Γ.

For the intensity, they specify a peak intensity due to all six beams. Thus to obtain the intensity per frequency component the peak intensity is divided by six for the laser beams. Then the intensity per frequency component is divided by the saturation intensity of 4.9 mW/cm^2 to obtain the saturation parameter. The peak intensities that are simulated are 46 mW/cm^2, 112 mW/cm^2, 229 mW/cm^2 and 456 mW/cm^2, which corresponds to saturation parameters of 1.56, 3.81, 7.79 and 15.51 respectively.

Parametrization of the CaF molecule

As explained in Section 4.2, PyLCP takes a parameterization to model the molecule. The parameters for the CaF simulations are stated in Table 4.4. These parameters are taken from the CaF example on the PyLCP website [4].

Magnetic field

In the article of Devlin and Tarbut, they are not specific about the magnetic field strength that is used in their simulations. After consulting J.A. Devlin via email he clarified that no magnetic field is used in the simulations of the 3D optical molasses. He claims that the counter propagation laser beams with different circular polarizations are sufficient to repump dark zeeman levels to bright states.

Name	value
Frosch and Foley a parameter	7.2 MHz
Rotational constant for X state	0.338 cm^{-1}
Rotational constant for A state	0.343 cm^{-1}
Isotropic spin-spin interaction	109.18 MHz
Anisotropic spin-spin interaction	40.12 MHz
Electron-spin rotational coupling constant	80.923 MHz

Table 4.4: Parameters for modeling X and A state of the BaF molecule in PyLCP. These parameters are taken from the CaF MOT example presented on the PyLCP website[4].

In the comparison, we show results with and without static magnetic field. The magnetic field is angled at 45 degrees to the polarization of the light.

Taking into account vibrationally excited states

For the laser cooling simulation, Devlin and Tarbutt consider the main cooling transition $A^2\Pi_{1/2} \rightarrow X^2\Pi^+(v = 0)$ and one vibrationally excited state $X^2\Pi^+(v = 1)$. Higher vibrational excitations are neglected. As explained in Section 2.4.3, the scattering rate is suppressed due to the presence of a vibrationally excited state. For reasons of computational load, they decided not to simulate the leaking to and repumping from the $X(v = 1)$ state. Instead, they make an estimation of the amount of molecules that are in the vibrationally excited state, this is then represented by a reduction factor η. The scattering rate and therefore the force is reduced by this factor, since molecules in a vibrationally excited state are not laser-cooled. Thus, the force is reduced by the factor η.

The forces resulting from the simulations are devided by η to mimic Devlin and Tarbut their approach to account for the vibrationally excited states. The factor η for 46 mW/cm^2, 112 mW/cm^2, 229 mW/cm^2, and 456 mW/cm^2 is 1.16, 1.32, 1.48, and 1.65 respectively.

4.6.1 Comparison

In Figure 4.15, each subplot shows simulations for a different intensity. For each intensity, a simulation is run for different magnetic field strengths. The black line in each plot is the data taken for Devlin and Tarbut [3].

The orange line in each plot results from the simulation without a magnetic field. This shows that no Doppler force is present without a magnetic field. The simulations by Devlin and Tarbut are also without magnetic field simulations, they claim that the laser polarizations are sufficient to account for dark state remixing. This is not the case in our simulations and would require additional research to find the reason behind this.

The rest of the lines are the results of simulations with different magnetic fields. This shows that the lack of Doppler force without the magnetic field is due to the lack of dark state remixing. The strength of the Doppler force is highly dependent on the strength of the magnetic field. For the two lower intensities, a magnetic field of 1 G results in a Doppler force similar to the result

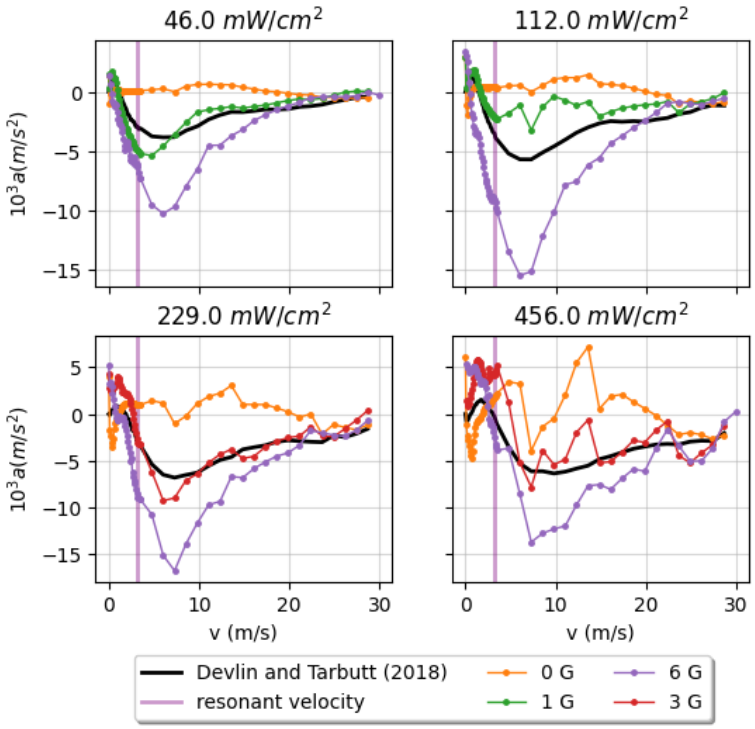

Figure 4.15: Simulation of 3D optical molasses of CaF, comparing to results of Devlin and Tarbutt (2018) [3] The four plots show different intensities. Each plot contains the result of Devlin and Tarbutt, and our simulation results for different magnetic field strengths.

of Devlin and Tarbut, while for the two higher intensities the Doppler force appears equal at $B = 3$ G.

Our results do show a resemblance to the results of Devlin and Tarbut in the velocity where the Doppler force peaks. Even though the peak is not the resonant velocity it is located at the same velocity of about twice the resonant velocity. Also, the rest of the shape of the Doppler force is similar.

At higher intensities, our Doppler force starts to fluctuate heavily while theirs remains constant. This shows that when our simulation of BaF starts to show fluctuating in the Doppler forces, this is probably due to the simulation technique instead of actual physics.

4.7 Conclusion and Outlook

In this section, the open-source Python package PyLCP is used to simulate the laser cooling experiment, which results in a velocity-force curve. For this study, we define two velocity regions: a high-velocity region to capture the maximum transverse velocity coming from the hexapole lens, and a low-velocity region, where we cool molecules to a transverse velocity suitable for the transverse acceptance of the interaction zone.

First, we determined the effect of the detuning, light intensity, and magnetic field on the Doppler

cooling force. The detuning dictates for what velocity the laser cooling force is strongest. The light intensity determines the strength of the Doppler cooling force and, due to power broadening, the width of the velocity region at which the Doppler cooling force is present. The magnetic field influences the strength of the laser cooling force and the appearance of the sub-Doppler forces.

For the two velocity regions, we find a laser cooling configuration that results in the best cooling. For the high-velocity region, from 4.5 m/s, we find an optimal detuning of $-1.5\ \Gamma$. This detuning has a resonant velocity of 3.6 m/s, which means that the peak of the Doppler force is just below the entry velocity. With a saturation between 7 and 11, which corresponds to a power between 31.5 mW and 49.5 mW, the transverse velocity of the molecules can be reduced to about 1.5 m/s.

For the low-velocity region, to 0.25 m/s, we find an optimal detuning between $-0.5\ \Gamma$ and $-1\ \Gamma$, which corresponds to a resonant velocity between 1.2 m/s and 2.4 m/s. We find that the magnetic field has a large effect on this velocity region due to the appearance of sub-Doppler forces at low magnetic field strengths. The optimal magnetic field is 2.5 G and the optimal saturation is between 7 and 11, the same as the high-velocity region. With this setup, the transverse velocity of the molecules can be reduced from about 1.5 m/s to 0.25 m/s.

The simulations do not include a vibrationally excited state, which would suppress the Doppler cooling force. For a future study, the effect of the vibrationally excited states can be incorporated.

Next, we study the effect of the magnetic field on the Doppler cooling force. The strength of the magnetic field and the angle between the magnetic field and light polarization determine the effectiveness of the dark state remixing. We find that for the high-velocity region, the optimal magnetic field is between 1.5 G and 2.5 G and that the Doppler force reduces quicker below this region than above this region. For the low-velocity region, the sub-Doppler forces have a large influence. Because of this, the optimal magnetic field strength is between 2.5 G and 4.5 G. In both velocity regions, we find that with a magnetic field parallel or perpendicular to the light polarization the Doppler cooling force is highly suppressed. The optimal angle is between 40 ° and 60 ° or between 110 ° and 140 °.

We also studied an alternative detuning strategy. Here we only detune one of the sidebands. The advantage is that no frequency component is blue-detuned from a transition, which could cause Doppler heating at high light intensity. We find that the Doppler forces peak at velocity below resonant velocity. We have not found an explanation for this. Because of this, the alternative detuning strategy did not show effectiveness for the high-velocity region. But for the low-velocity region, it showed more potential.

At last, we benchmark the simulation method against the results of a CaF 3D MOT simulation by J.A. Devlin and M.R. Tarbutt (2018) [3]. We simulate the same setup and compared the velocity-force curve to their results. Devlin and Tarbut did not use a static magnetic field for Larmor Precession, instead different light polarizations cause dark state remixing. This could not be reproduced in our simulations, although the polarization of light is identical to the one described in the article of Devlin and Tarbut we did not see a Doppler curve without a magnetic field. Then we compared their simulations result to a simulation with a magnetic field. From

this, we find that the shape of the Doppler cooling force is similar, and the location of the peak is identical. But the height of the Doppler cooling force is different, this is probably due to a different remixing rate.

For a future study, it is interesting to look into why dark state remixing with just the polarized light does not work in our simulations. This would allow for a better comparison of the Doppler cooling force strength.

5. Summary

In this thesis, we present a study on the laser cooling of BaF. First, the concept of Doppler cooling and sub-Doppler cooling is explained. Then the energy level structure is introduced and all aspects important to laser cooling are highlighted, such as the existence of vibrationally excited states. Then we introduce the laser cooling scheme, which determines in what velocity region the Doppler cooling force is focussed and how the scattering rate can be maximized.

In the second chapter, we develop a method to reintroduce molecules from the vibrationally excited states back to the laser cooling cycle, called vibrational repumping. For the first vibrationally excited state, a laser is tuned such that molecules are excited to $B^2\Sigma^+$ from which they decay to the ground state of the laser cooling transition. For the second vibrationally excited state, molecules are pumped to the first vibrationally excited via $A^2\Pi_{1/2}(v = 1)$. Sidebands are added to the laser by an electro-optical modulator (EOM). The modulation depth and driving frequency of the EOM are tuned such that the sidebands overlap with hyperfine transitions of $X^2\Sigma^+(v = 1) \rightarrow B^2\Sigma^+(v = 0)$.

In the last chapter, simulations are used to gain insight into the effect of the light intensity, detuning, and magnetic field on the Doppler force. We study the optimal laser cooling configuration for a low-velocity region and a high-velocity region. We find that laser cooling molecules from 4.5 m/s with an interaction time of 0.8 m/s, the lowest velocity can be reached with a detuning if -1.5 Γ. And when laser cooling molecules to 0.25 m/s the optimal detuning is -1 Γ. No additional cooling is gained when using lower detuning. For the light intensity, we found that Doppler cooling works best between 7 and 9 times saturation. In the experiment, this equates to a laser power between 31.5 mW and 40.5 mW for a laser beam with a $1/e^2$ radius of 10 mm.

We study the effectiveness of an alternative detuning strategy. By detuning just one sideband, we don't suffer from sidebands blue-detuned from a transition. We find that the Doppler force is most prominent for low velocities.

At last, we benchmark the simulation method used in our studies to a published result of a 3-dimensional optical molasses of CaF by J.A. Devlin and M.R. Tarbutt (2018). We find that the shape of the Doppler cooling force is similar but there is a difference in the magnitude of the cooling force. We find that a possible explanation for the difference is the rate of remixing dark Zeeman sublevels. In the article Devlin and Tarbutt use opposite polarized laser light for remixing, in our simulation this effect does not result in remixing. Instead, we use a magnetic field for remixing, but the strength of the magnetic field highly influences the Doppler cooling strengths. This makes a direct comparison challenging.

Acknowledgements

I would like to thank my supervisor Steven Hoekstra for the opportunity to work with the fascinating experimental setup of the NL-eEDM collaboration. I feel privileged to have worked on such a profound and class-leading experiment. Also, I would like to thank my daily supervisor Joost W.F. van Hofslot for his support during my master's project. Joost taught me many things about laser cooling and guided me toward a research subject. I enjoyed our sessions in the lab. At last, I would like to thank the NL-eEDM Groningen group for the enjoyable meetings and outings.

A. Simulation results for all configurations

A.1 Optimum force curve

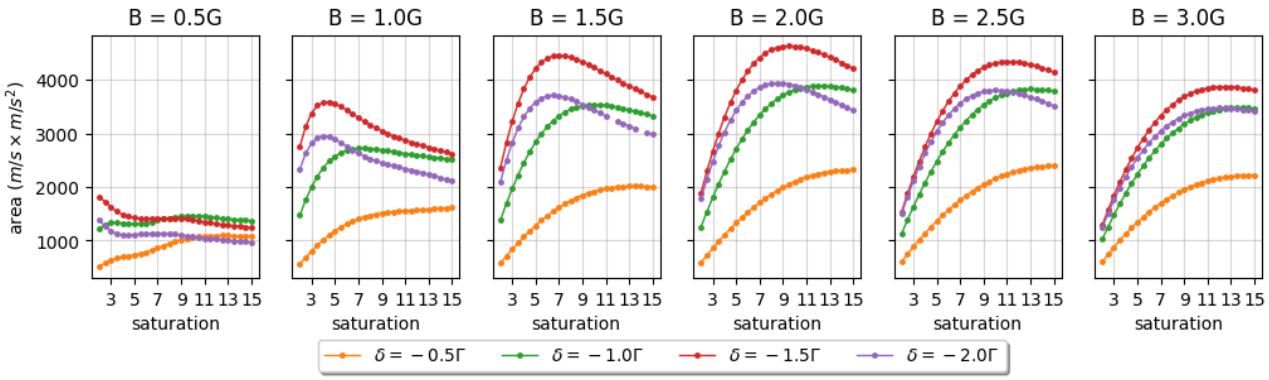

Figure A.1: The area under the velocity-force curve between 3.5 m/s and 4.5 m/s, each plot is for a different magnetic field strength. Each plot shows the result for three different detunings. This figure extends Figure 4.4 with all simulated configurations.

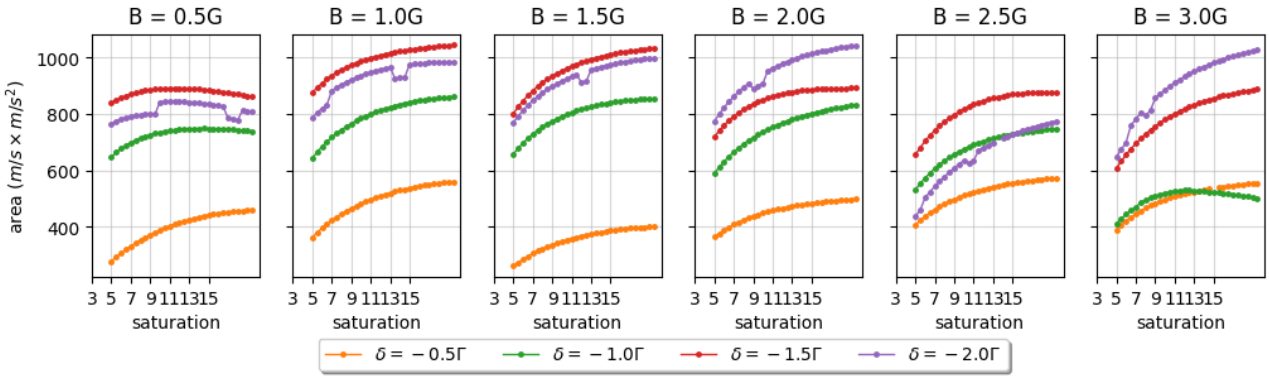

Figure A.2: The area under the velocity-force curve between 0.25 m/s and 1 m/s, each plot is for a different magnetic field strength. Each plot shows the result for three different detunings. This figure extends Figure 4.5 with all simulated configurations.

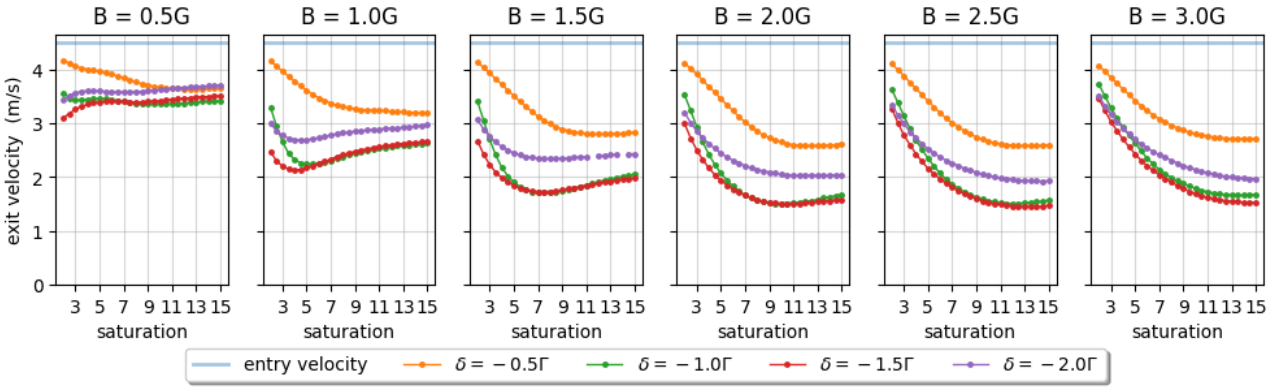

Figure A.3: The exit velocity to which a particle can be cooled which enters the cooling section with a velocity of 4.5 m/s. This figure extends Figure 4.6 with all simulated configurations.

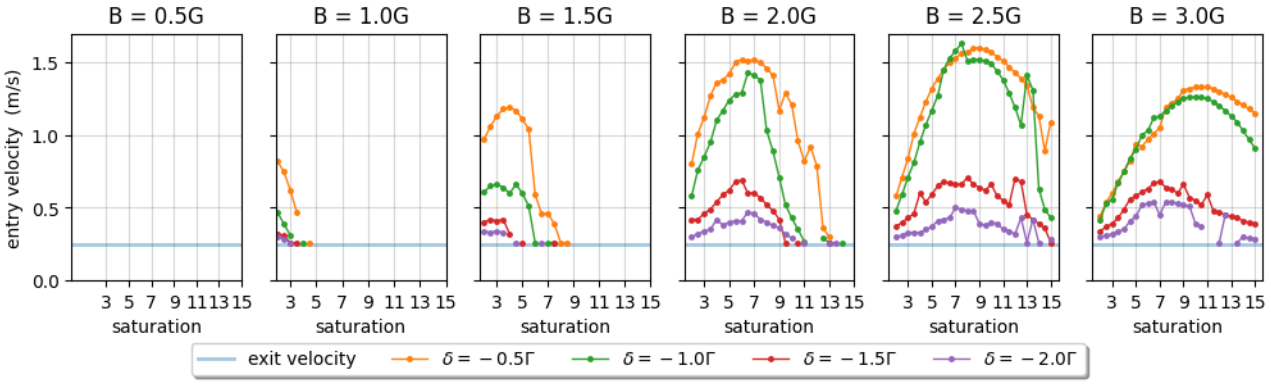

Figure A.4: Maximum start velocity such that the molecule can be cooled to 0.25 m/s within the laser cooling region. For some configurations, it is not possible to reach this velocity because the acceleration is positive for low velocities. This figure extends Figure 4.7 with all simulated configurations.

B. Practical additions to the experimental setup

B.1 Grafana and influxdb for live dashboarding

Various parameters of the laser cooling experiment are constantly monitored, such as temperatures, pressures, flow rates, and laser frequencies. There was a need for a clear dashboard that could be accessed via the web such that the data is visible from anywhere.

We created a Grafana application with an influxdb database hosted on a Kubernetes server of the University of Groningen [14, 16, 18]. Grafana is a tool for easy setup of clear dashboards and influxdb is a database system specifically for timestamped data.

The Grafana dashboard is a replacement for an existing primitive dashboard, so most of the data acquisition technology was already set up. We could hook into the existing code to send data to the influxdb database.

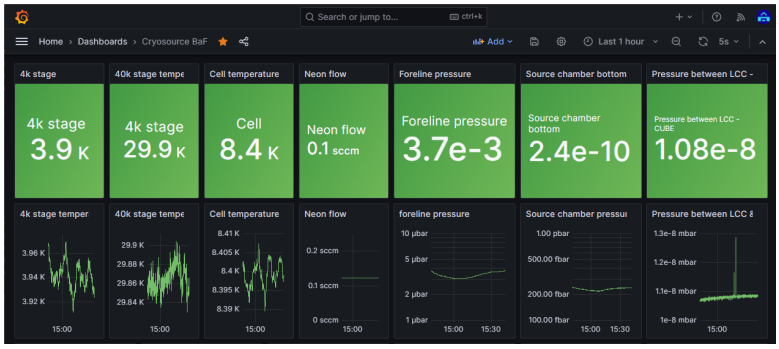

Figure B.1: A single row of parameters is shown in the Grafana dashboard. For each parameter, the latest value is shown in the green block, and a graph of the recorded values in the last hour.

The Grafana dashboard, shown in figure B.1, is an array of large numbers and graphs. The large numbers show the latest value of the parameters, allowing for a quick overview of the state of the experiment. The graphs, show parameter values over the last period of time. The exact period can be changed by the user.

B.2 TTL Pulse or gate for camera trigger combination

The experiment uses an Andor iXon DU897 Electron Multiplying CCD (EMCCD) camera. During each cycle of the experiment, the EMCCD camera makes three images. One image is for the detection of the molecules, one is for background detection, and one image is for calibration purposes. Each image is externally triggered by TTL pulses generated by a trigger

box. The pulses come from three different channels on a BNC trigger box. The three pulses must be combined into one before it can enter the EMCCD camera.

For this purpose, I made a BNC OR gate that can combine TTL pulses from three different BNC cables into one. The OR GATE uses a TEXAS INSTRUMENTS SN74F32N surrounded by a 3D-printed housing. Figure B.2 shows a schema of the designed OR Gate and a picture.

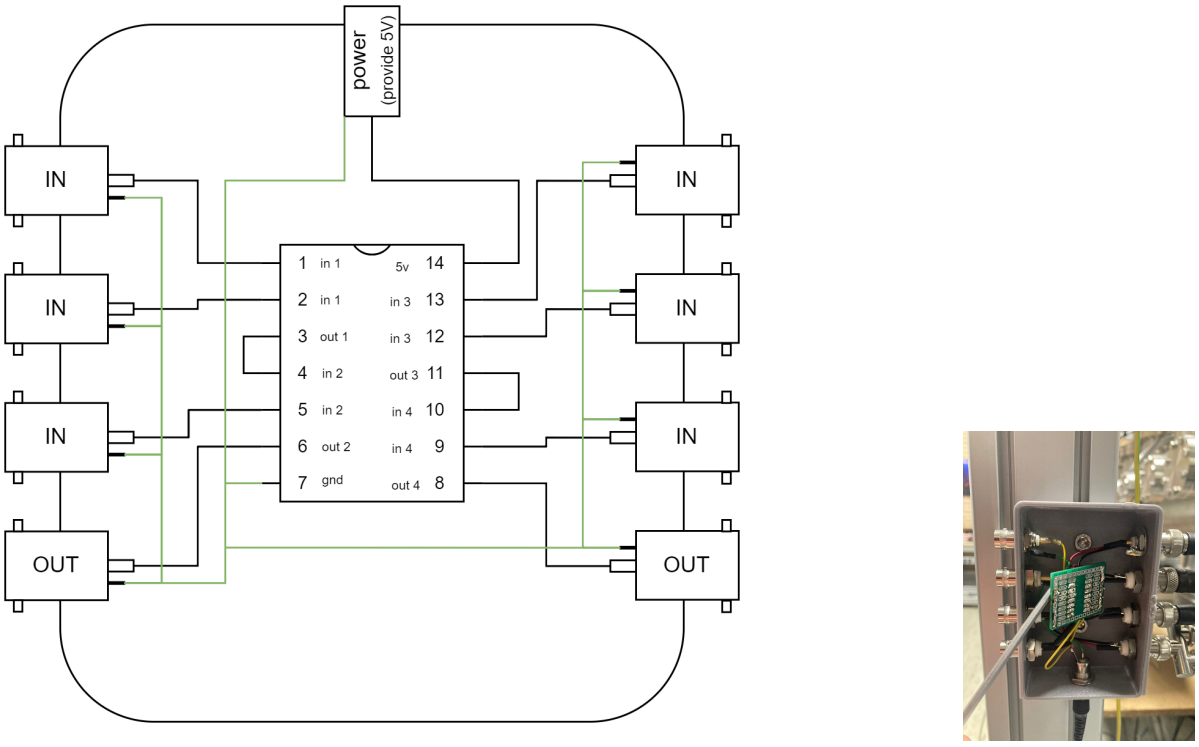

(a) **(b)**

Figure B.2: (a) Schema of the homemade OR gate. The green lines denote ground lines. (b) Picture of the homemade OR gate, with the lid removed.

B.3 Mounting the photon multiplier tube above detection cube

We installed an extra photon multiplier tube (PMT) above the vibrational recovery section of the experiment. The PMT was already shown in Figure 2.5 denoted by PMT2. A PMT is a time-sensitive device that detects laser-induced fluorescence to single photon precision.

The extra PMT allows us to detect the existence of molecules at the end of the experiment and record their time of arrival. With the addition of an extra PMT at the end of the laser cooling experiment more information about the molecules can be extracted, for example, the longitudinal velocity of the molecules. Also, it allows us to find transition frequencies by performing spectroscopy as seen in Figure 2.2.

The PMT is attached to three orthogonal translation stages to allow for easy adjustments to the position of the PMT. Which can be seen in Figure B.3a

The fluorescence is focussed on the PMT by a lens system, the schematic of which is shown in Figure B.3b. The 712 nm filter allows for background-free detection of the $B^2\Sigma^+_{1/2} \rightarrow X^2\Sigma^+_{1/2}(v = 0)$ transition, which is important in the recovery of molecules in $X^2\Sigma^+_{1/2}(v = 0)$.

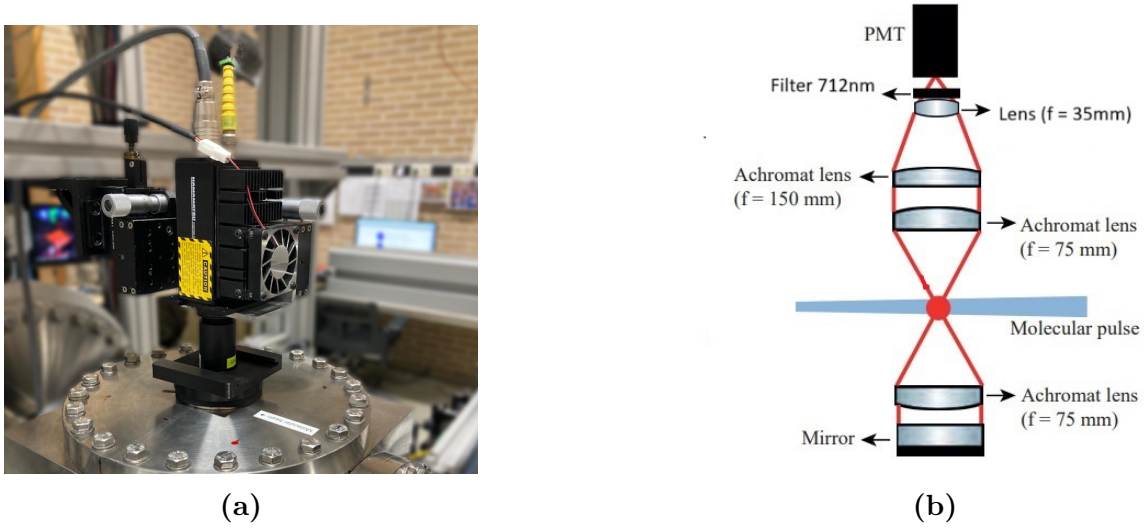

(a) **(b)**

Figure B.3: (a) Picture of the photon multiplier tube suspended by three orthogonal transition stages (b) The lens system in front of the photon multiplier tube to focus the fluorescence on the photon multiplier tube. Image from [1] (edited)

Bibliography

[1] Parul Aggarwal. *Production, deceleration and trapping of SrF molecules*. [Groningen]: University of Groningen, 2021. DOI: 10.33612/diss.177484581.

[2] Ralf Albrecht et al. "Buffer-gas cooling, high-resolution spectroscopy, and optical cycling of barium monofluoride molecules". In: *Physical Review A* 101.1 (Jan. 2020), p. 013413. DOI: 10.1103/PhysRevA.101.013413. URL: https://link.aps.org/doi/10.1103/PhysRevA.101.013413 (visited on 04/17/2024).

[3] J. A. Devlin and M. R. Tarbutt. "Laser cooling and magneto-optical trapping of molecules analyzed using optical Bloch equations and the Fokker-Planck-Kramers equation". en. In: *Physical Review A* 98.6 (Dec. 2018), p. 063415. ISSN: 2469-9926, 2469-9934. DOI: 10.1103/PhysRevA.98.063415. URL: https://link.aps.org/doi/10.1103/PhysRevA.98.063415 (visited on 04/15/2024).

[4] S Eckel et al. *PyLCP CaF MOT example*. URL: https://python-laser-cooling-physics.readthedocs.io/en/latest/examples/MOTs/20_CaF_MOT.html (visited on 04/06/2024).

[5] S. Eckel et al. "PyLCP: A python package for computing laser cooling physics". In: (2020). DOI: 10.48550/ARXIV.2011.07979. URL: https://arxiv.org/abs/2011.07979 (visited on 02/19/2024).

[6] NL-eEDM Collaboration et al. "Benchmarking of the Fock-space coupled-cluster method and uncertainty estimation: Magnetic hyperfine interaction in the excited state of BaF". In: *Physical Review A* 105.5 (May 2022), p. 052811. DOI: 10.1103/PhysRevA.105.052811. URL: https://link.aps.org/doi/10.1103/PhysRevA.105.052811 (visited on 05/30/2024).

[7] *Electro-Optic Modulators - Thorlabs*. en. URL: https://www.thorlabs.com (visited on 06/28/2024).

[8] *electron-EDM*. nl. Nov. 2016. URL: https://www.rug.nl/research/vsi/newtopics/electron-edm (visited on 06/28/2024).

[9] Yohei Ema, Ting Gao, and Maxim Pospelov. "Standard Model Prediction for Paramagnetic Electric Dipole Moments". In: *Physical Review Letters* 129.23 (Nov. 2022), p. 231801. DOI: 10.1103/PhysRevLett.129.231801. URL: https://link.aps.org/doi/10.1103/PhysRevLett.129.231801 (visited on 06/17/2024).

[10] Wolfgang Ernst, Jörn Kändler, and T. Törring. "Hyperfine Structure and Electric Dipole Moment of BaF $X^2\Sigma+$". In: *The Journal of Chemical Physics* 84.9 (1986), pp. 4769–4773. ISSN: 1089-7690. DOI: 10.1063/1.449961.

[11] Kevin Esajas. "Intense slow beams of heavy molecules to test fundamental symmetries". PhD thesis. [Groningen]: University of Groningen, 2021. DOI: 10.33612/diss.170215126. URL: https://fse.studenttheses.ub.rug.nl/21420/1/mPHYS_2019_RutgerHof.pdf.

[12] N. J. Fitch and M. R. Tarbutt. "Laser cooled molecules". In: vol. 70. arXiv:2103.00968 [physics]. 2021, pp. 157–262. URL: http://arxiv.org/abs/2103.00968 (visited on 05/21/2024).

[13] C. J. Foot. *Atomic Physics*. en. Google-Books-ID: _CoSDAAAQBAJ. Oxford University Press, 2005. ISBN: 9780198506959.

[14] *Grafana: The open observability platform*. en. URL: https://grafana.com/ (visited on 06/05/2024).

[15] Yongliang Hao et al. "High accuracy theoretical investigations of CaF, SrF, and BaF and implications for laser-cooling". In: *The Journal of Chemical Physics* 151.3 (July 2019). arXiv:1904.02516 [physics, physics:quant-ph], p. 034302. ISSN: 0021-9606, 1089-7690. DOI: 10.1063/1.5098540. URL: http://arxiv.org/abs/1904.02516 (visited on 04/05/2024).

[16] *InfluxDB — Real-time insights at any scale*. Jan. 2022. URL: https://www.influxdata.com/home/ (visited on 06/05/2024).

[17] L. B. Knight, W. C. Easley, and W. Weltner. "Hyperfine interaction and chemical bonding in MgF, CaF, SrF, and BaF molecules". In: 54 (1971), p. 322.

[18] *Kubernetes*. en. URL: https://kubernetes.io/ (visited on 06/05/2024).

[19] LHCb collaboration et al. "LHCb Detector Performance". In: *International Journal of Modern Physics A* 30.07 (Mar. 2015). arXiv:1412.6352 [hep-ex], p. 1530022. ISSN: 0217-751X, 1793-656X. DOI: 10.1142/S0217751X15300227. URL: http://arxiv.org/abs/1412.6352 (visited on 06/17/2024).

[20] Virginia Rose Marshall. *Spectroscopy and Systematic Effects: an eEDM experiment using BaF molecules*. [Groningen]: University of Groningen, 2024. DOI: 10.33612/diss.972290628.

[21] H. Mohanty, J. C. Mohanty, and B. S. Mohanty. "Franck-Condon factors, r-centroids & intensity distributions in some band systems of BaF molecule". In: 8 (1970), p. 423.

[22] E. S. Shuman, J. F. Barry, and D. DeMille. "Laser cooling of a diatomic molecule". en. In: *Nature* 467.7317 (Oct. 2010), pp. 820–823. ISSN: 1476-4687. DOI: 10.1038/nature09443. URL: https://www.nature.com/articles/nature09443 (visited on 02/19/2024).

[23] Anno Touwen et al. "Manipulating a beam of barium fluoride molecules using an electrostatic hexapole". In: (2024). DOI: 10.48550/ARXIV.2402.09300. URL: https://arxiv.org/abs/2402.09300 (visited on 04/17/2024).

[24] Meng Xia et al. "Destabilization of dark states in MgF molecules". In: *Physical Review A* 103.1 (Jan. 2021), p. 013321. DOI: 10.1103/PhysRevA.103.013321. URL: https://link.aps.org/doi/10.1103/PhysRevA.103.013321 (visited on 06/15/2024).